Gönnert, Gabriele; Dube, Shishir K.; Murty, Tad; Siefert, Winfried

4. Special Hydrodynamic Problems

Die Küste

4. Special Hydrodynamic Problems

4.1 Tides

Tide is the rise and fall of the sea surface due to gravitational forces. To following material based on LEBLOND and MYSAK (1978) and GODIN (1972, 1980a, 1980b, 1988, 1991, 1996), IHP-OHP (1987, 1991), DEAN (1966), DIETRICH et al. (1975), DEFANT (1961).

An extremely useful qualitative description of some tidal phenomena is obtained by considering the equilibrium shape that a layer of water on a spherical earth would assume under the action of a tide-producing body. This is the "Equilibrium Theory of Tides", presented by Darwin in 1898 and describing the tides as those water fluctuations apparent to an observer traversing along a constant latitude line through the stationary and deformed water layer.

To describe the tides in a more realistic manner, dynamic aspects of the tidal waves in the oceanic basins and on a rotating earth must be considered. It is well known that the oceanic tides arise mainly from the attractions of the moon and sun. Although the moon is a much smaller body than the sun, it exerts a stronger influence in generating oceanic tides because of its proximity to the earth. The effects of submarine and coastal topography in altering the tidal features, resonance in bays and estuaries, and forces due to the rotating earth all contribute to tidal features, which define the complete mathematical "cause and effect" description. Therefore an extensive discussion of the theory of tides exists.

Table 4.1: Tidal constituents usually required for determining the tide at a given location. Note that this is only a small part of a rather lengthy list, most of which is generally irrelevant for storm surge-tide interaction purposes

Nature of constituent	Symbol for constituent	Frequency (degrees.h^{-1})	Period (h)
Semidiurnal	M_2	28.98	12.42
Semidiurnal	N_2	28.44	12.66
Semidiurnal	S_2	30.00	12.00
Semidiurnal	K_2	30.08	11.97
Diurnal	O_1	13.94	25.82
Diurnal	K_1	15.04	23.94
Diurnal	P_1	14.96	24.06

Following GODIN (1980a, 1980b), the vertical component z (t) of the tide is defined as follows:

$$z(t) = zo + \sum_{j=1}^{n} A_j \cos(\sigma_j t - a_j) \qquad (4.1)$$

where, z_o is a constant that denotes the reference level, which is chosen such that the observed water level rarely, if ever, falls below z_o, and the other term on the right is a summation of *n* constituents of amplitude Aj, frequency σ_j, and phase a_j where j varies from 1 to *n*. Note that the frequencies yj of the constituents are the same for any tidal record (for the same constituent); however, the amplitude and phase of the constituent might vary from one tidal station to another. Through a harmonic analysis of the observed tidal record, one can determine the amplitudes and phases of the various tidal constituents. In principle, the total number of

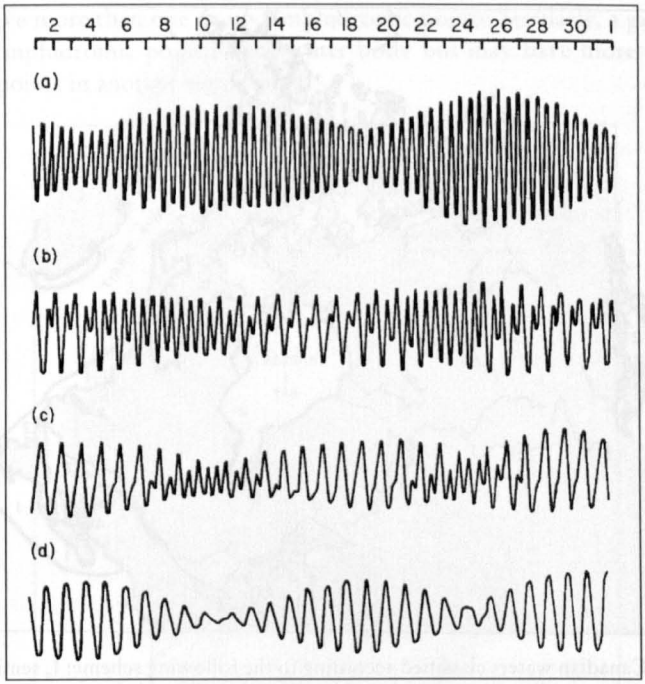

Fig. 4.1: Schematic representation of a 1-mo-long tidal record. (a) Semidiurnal; (b) mixed, mainly semidiurnal; (c) mixed, mainly diurnal; (d) diurnal

constituents could be as high as 500, but rarely must one use more than a dozen or so of the important constituents in representing a tidal record.

As described above, the tide is the rise and fall of the sea's surface. The flowing to and fro is called tidal current. The tide is a wave period of about 12.4 hours, the semi-diurnal tide, or of about 24.8 hours (diurnal tide) or of varying periods (mixed tides). The most important of the semidiurnal and diurnal tidal constituents that are needed in representing an observed tidal record are listed in Table 4.1.

In practical tidal studies, it was found convenient to classify the tides into these four types: semidiurnal, mixed-mainly semidiurnal, mixed-mainly diurnal, and diurnal. A tide is referred to as semidiurnal if there are two high waters and two low waters daily of roughly the same amplitude (Fig. 4.1a). Mixed tides of the mainly semidiurnal type have two high waters and two low waters with the amplitudes being unequal (Fig. 4.1b). Mixed tides of the mainly diurnal type are said to exist if at times there is only one high water and one low water per day and at other times there are two large inequalities (Fig. 4.1c). For diurnal tides, there is one high water and one low water per day (Fig. 4.1d).

Three examples will be shown with this classification. First DOHLERS (1967) has classified the Canadian waters according to this scheme in Fig. 4.2, second EASTON (1970) for Australia (Fig. 4.3) and third PRIDA (1990, personal communication, quotation from IHP-OHP-BERICHTE 1991) (Fig. 4.4).

A cotidal chart is a convenient way of presenting tidal information for each tidal constituent separately. Two sets of lines exist on a cotidal chart. Corange (coamplitude) lines represent contours of the range (amplitude) of the constituent, whereas cophase lines represent the contours of equal phase (usually with reference to Greenwich, expressed in degrees per

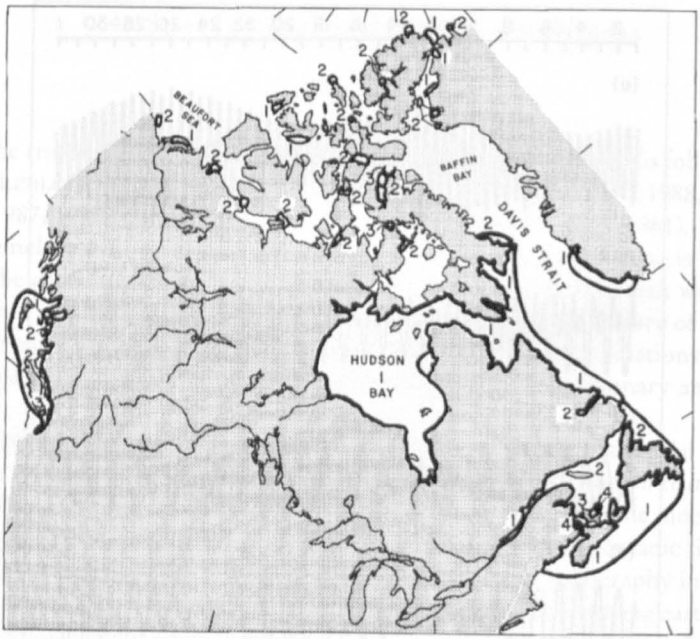

Fig. 4.2: Tides in Canadian waters classified according to the following scheme: 1, semidiurnal; 2, mixed, mainly semidiurnal; 3, mixed, mainly diurnal; 4, diurnal. (DOHLER, 1967)

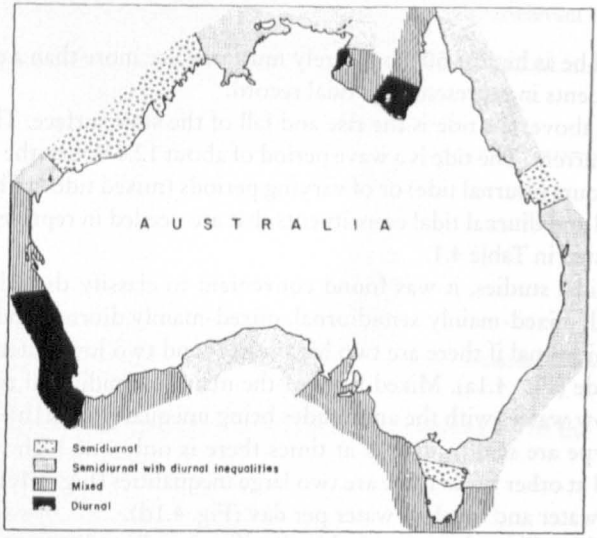

Fig 4.3: Tidal types along the Australian coast (EASTON, 1970)

hour). Amphidromic points, which appear for certain constituents in water bodies, are the locations where the range (amplitude) of the particular constituent is zero. Thus, it is basically a node for the vertical motion, the nodal line becoming just a point either due to the presence of transverse motion or due to the influence of the earth's rotation (GEORGE, 1980). In a water body, one tidal constituent may have an Amphidromic point, whereas another con-

stituent may have more than one or no Amphidromic points. Similarly, a given constituent may have an Amphidromic point in one water body but may have more than one or no Amphidromic points in another water body.

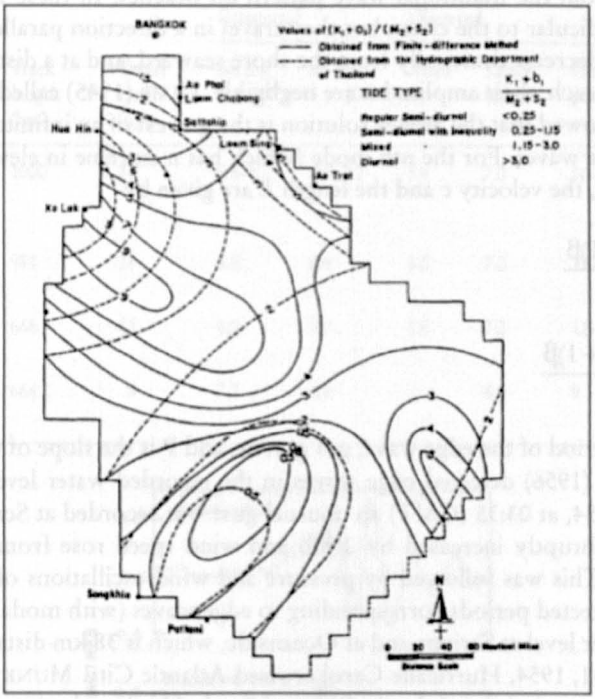

Fig. 4.4: Types of tide in the Gulf of Thailand (Prida, personal comment, quotation from IHP-OHP-BERICHTE, 1991)

4.2 Resonance, Edge Waves

The topic of resonance, although relevant to storm surges, is so vast that it cannot be considered in detail here.

Any water body, such as a lake, inlet, bay, gulf, or a continental shelf, has natural modes of oscillation whose periods are determined by the geometry of the water body and the water depth. A knowledge of the natural modes of the water body is quite important in determining whether a given storm surge will be amplified or not and in determining the detailed characteristics of the surge in a particular water body for a given forcing.

For convenience, this section will be divided into three subsections: in the first subsection the theory of seiches will be described in some detail; in the second subsection the Helmholtz mode will be considered; in the final subsection the correct boundary conditions at the open part of the water body will be discussed.

Edge Waves and Their Role in Storm Surges

The literature on the topic of edge waves has grown enormously in recent times, and the reader is referred to LEBLOND and MYSAK (1978) and MURTY (1977) for a review. Here, edge

waves will be considered strictly for the role they play in storm surges; discussion will not deal with the general phenomenon of edge waves.

STOKES (1847) obtained solutions for wave motion over a sloping beach, these solutions being different from the traditional wave pattern on beaches. In these new solutions, the crests are perpendicular to the coast, but they travel in a direction parallel to the coast and their amplitudes decrease drastically from the shore seaward, and at a distance of one wavelength from the beach, their amplitudes are negligible. LAMB (1945) called them edge waves. URSELL (1952) showed that the Stokes solution is the gravest of an infinite number of possible modes of edge waves. For the nth mode (which has n extreme in elevation between the coast and the sea), the velocity c and the length L are given by

$$c = \frac{gT\sin(2n+1)\beta}{2\pi} \tag{4.2}$$

$$L = \frac{gT^2\sin(2n+1)\beta}{2\pi} \tag{4.3}$$

where, T is the period of the edge wave, g is gravity, and P is the slope of the beach.

MUNK et al. (1956) detected edge waves in the recorded water levels at Scripps Pier. On January 6, 1954, at 03:35 (GMT) an unusual gust was recorded at Scripps Pier. Atmospheric pressure abruptly increased by 2 mb and wind speed rose from 3 to 14 mi – h-' (4.8-22 km.h-1). This was followed by pressure and wind oscillations of an 8-min period. These authors detected periods corresponding to edge waves (with modal number n = 1) in the recorded water level at Scripps and at Oceanside, which is 38 km distant.

On August 31, 1954, Hurricane Carol crossed Atlantic City. MUNK et al. (1956) computed the edge wave modes at Atlantic City and Sandy Hook and compared the calculated periods with observed periods. The main result is that the edge wave periods are largely due to the gently sloping bottom. The longest edge wave period is associated with the fastest hurricane.

MUNK et al. (1956) also computed the edge wave modes for Osaka Bay, Japan, over which a storm passed on August 29, 1953. The bottom slope in Osaka Bay is about 15 times greater than that of the New Jersey coast. Hence, the periods of edge waves in Osaka Bay should be about 1/15 those on the New Jersey coast, and this result is supported by observations.

GREENSPAN (1970) did a theoretical study of edge waves in an exponentially stratified fluid. He showed that the first mode is completely insensitive to the density field. Stratification modifies the range of existence of higher modes.

On June 26, 1954, a squall line passed over the southern part of Lake Michigan and caused a surge on the Chicago waterfront. Several people were killed. This was explained by resonant coupling between the squall line and the resulting gravity waves generated in the lake (DONN and EWING, 1956). A resurgence (i.e. reflection of the waves from the eastern shore of the lake) explains its unexpected arrival at Chicago some 2 h after the squall line had passed.

On July 6–7, 1954, another squall line crossed Lake Michigan from north to south with an average speed of 50 mi. h-' (80.5 km. h-'). Long-period waves were recorded at several locations following this squall line. DONN and EWING (1956) invoked edge waves to account for these water level disturbances. The time of arrival of the squall line and the magnitude of the pressure change at several stations are listed in Table 4.3, and the travel time curves of the

Table 4.2: Periods and durations of edge waves generated by four hurricanes. (MUNK et al., 1956)

Hurricane	Velocity U (km.h^{-1})	Track length (km)	Travel time (h)	Wave period T (h) Computed $\sin\beta = 5 \times 10^{-4}$	Computed $\sin\beta = 5 \times 10^{-4}$	Observed Atlantic City	Observed Sandy Hook	Duration (h) Computed	Observed Atlantic City	Observed Sandy Hook
Aug. 30–Sept. 1 (Carol)	59–63	1000	24	5.8–6.1	6.9–7.2	5.5	7.0	16–24	20	26
Sept. 11–12, 1954 (Edna)	59	981	24	5.8	6.9	6.0	7.0	17–24	23	?
Sept. 14–15, 1944	61	666	12	6.0	7.1	5.6	7.2	11–12	23	30
Sept. 21–22, 1938	74	666	9	7.3	8.6	–	8.0	9	–	16

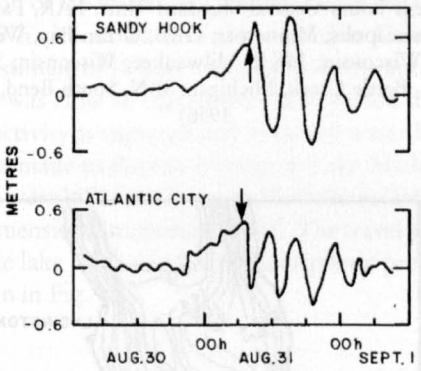

Fig. 4.5: Storm surges at Sandy Hook and Atlantic City, New Jersey, during Hurricane Carol of August 30–September 1, 1954. Arrows indicate the time of passage of the storm centre. (MUNK et al., 1956)

Table 4.3: Time of occurrence and pressure change for the squall line of July 6, 1954, in the United States. (DONN and EWING, 1956)

Station name	Station code	State	Time (CST) of occurrence of pressure change	Magnitude of Pressure change (mb)
Fargo	FAR	North Dakota	06:50	2.03
St. Cloud	STC	Minnesota	08:39	3.05
Minneapolis	MSP	Minnesota	09:54	2.37
Green Bay	GRB	Wisconsin	11:00	1.36
Traverse City	TVC	Michigan	12:30	0.68
Madison	MSN	Wisconsin	13:02	2.71
Milwaukee	MKE	Wisconsin	13:24	2.03
Muskegon	MKG	Michigan	14:00	1.36
Chicago	CHI	Illinois	15:30	3.39
Battle Creek	BTL	Michigan	15:30	1.36
South Bend	SBN	Indiana	15:55	2.03

squall line are shown in Fig. 4.6. The abbreviations for the stations shown in this diagram are the same as in Table 4.3. The water level records from Waukegan, Wilson Avenue (Chicago), Calumet Harbour (Chicago), and Ludington (see Fig. 4.7) were used.

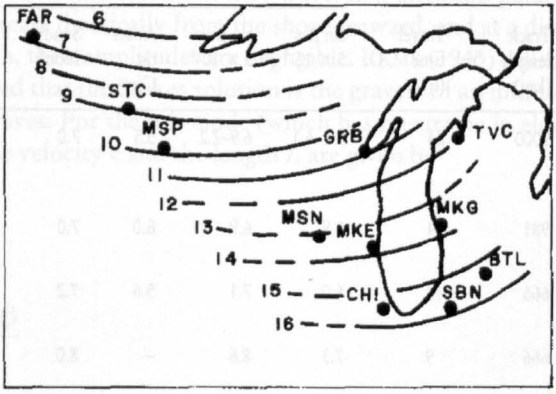

Fig. 4.6: Travel time curves (isochrones) of the squall line on July 6, 1954, over Lake Michigan and surroundings. Numbers represent hours Central Standard Time. FAR, Fargo, North Dakota; STC, St. Cloud, Minnesota; MSP, Minneapolis, Minnesota; GRB, Green Bay, Wisconsin; TVC, Traverse City, Michigan; MSN, Madison, Wisconsin; MKE, Milwaukee, Wisconsin; MKG, Muskegon, Michigan; CHI, Chicago, Illinois; BTL, Battle Creek, Michigan; SBN, South Bend, Indiana. (DONN and EWING, 1956)

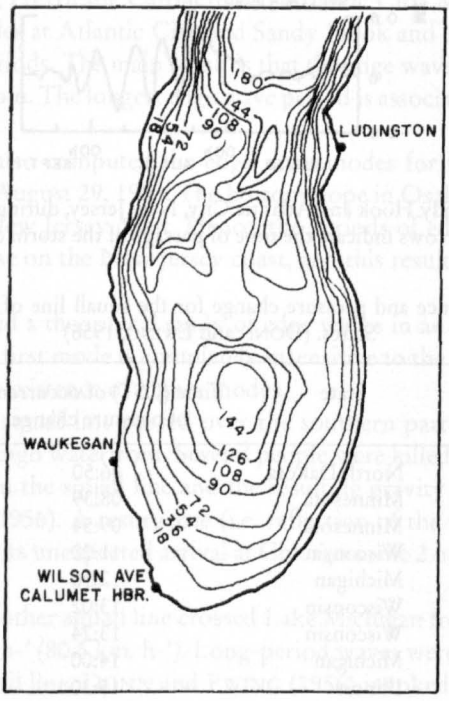

Fig. 4.7: Bottom topography of the southern port of Lake Michigan and the water level stations used in the study. (DONN and EWING, 1956)

The pertinent meteorological and water level data at these four stations are summarised in Table 4.4. It can be seen from Fig. 4.7 that the depth increases more or less uniformly with distance from the shore. The distance (i.e. X/21r) at which the edge wave amplitude should be negligible is about 16 mi (25.6 km). Starting just north of Chicago to up to 50 mi (80.5 km) north of Waukegan, the bottom slope was determined to the 300-ft (91.4 m) contour at six different locations. These values (i.e. of sin P) were 0.0016, 0.0021, 0.0024, 0.0035, 0.0034, and 0.0029. For the phase velocity c of the edge wave a value of 72.5 ft. s-' (22 m. s-') was used. This gives from eq. (4.2) (for n = 1) a period of 103 min. From Table 4.4 the average period is 109 min. Thus, the calculated period of edge waves agrees with the observed period.

Calculations gave values of 50 mi. h^{-1} (80.4 km. h^{-1}) and 61 mi. h^{-1} (98 km. h^{-1}), respectively, for the edge wave velocity in the northern and southern parts of Lake Michigan. Since the speed of travel of the squall line was 50 mi. h^{-1} (80.4 km. h^{-1}), resonance transfer of energy occurred from the squall line to the gravity waves in the water. At Ludington, the bottom topography precludes generation of edge waves. Hence, just after the passage of the squall line (at 1:00 p.m.) the amplitudes of the water waves were small. However, at 8:00 p.m. much larger waves appeared at Ludington. This was explained due to the reflected larger waves from other areas travelling towards Ludington.

The observed duration of the water level disturbance in the Chicago – Waukegan area is estimated to be about 29 h. About 20 h of this record at Calumet Harbour is shown in Fig. 4.8. The theoretical estimate of 18 h for the edge wave duration is somewhat smaller. The period of the edge waves was close to that of the seiche period in the southern part of Lake Michigan; hence, seiche activity is expected and observed water levels confirm this.

Earlier, reference was made to the storm surge in Lake Michigan due to a squall line on June 26, 1954 (six persons were killed in Chicago). PLATZMAN (1958a) studied this surge using a time-dependent two-dimensional numerical model. The travel time curves of this squall line are shown in Fig. 4.9. The lake level, wind, and atmospheric pressure at the Wilson Avenue crib in Chicago are shown in Fig. 4.10.

Table 4.4: Arrival time of pressure jump and first wave of surge and wave periods and duration of the water level disturbance at four stations in Lake Michigan associated with the squall line of July 6, 1954. (DONN and EWING, 1956)

Station	Pressure jump arrival time (CST)	Time of arrival of first wave of surge (CST)	Period (min)[a] Long-period waves	Period (min)[a] Short-period waves	Duration of wave disturbance (h)
Waukegan (Illinois) Wilson Ave. (Chicago)	~15:00	15:30	110–120	20	29
Calumet Harbour (Chicago)	15:30	15:30	97–100	18–20	29
Ludington (Michigan)	15:30	15:30	115	20	–[b]
	~13:00	20:00–22:00	84	–	–[b]

[a] Not to be confused with wind waves whose periods are of the order of a few seconds.
[b] Record incomplete.

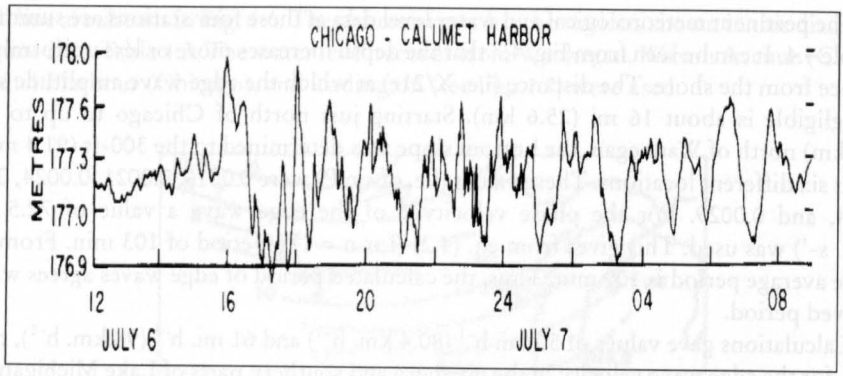

Fig. 4.8: Water level disturbance at Chicago's Calumet Harbour during July 6–7, 1954. (DONN and EWING, 1956)

PLATZMAN made five computations, i.e. using five different speeds of propagation for the squall line. These were 42, 48, 54, 60 and 66 knots (1 knot = 1.85 km – h-'). In each of these five computations he took the direction of propagation of the squall line as north-west to south-east, the width of the squall line as 10 nautical miles (18.5 km) and the magnitude of the pressure rise as 4 mb. The observed and computed results are compared in Table 4.5. In interpreting these results, it should be noted that the computations include atmospheric pressure gradient as a forcing term, but not wind stress. (Also, the Coriolis terms were ignored, although this omission may not be significant.)

PLATZMAN (1958a) summarised the results at the Wilson Avenue crib as follows:

1) The computed amplitude of the main (reflected) surge is approximately one-half the observed amplitude, but the inclusion of wind stress probably will remove this discrepancy.
2) The computed phases between significant events (Table 5.6) are in good agreement with the observations.
3) The structure of the tail of the reflected surge (and probably also the primary surge) is not in agreement with the observed structure, probably because the resolving power of the grid is inadequate for this purpose.

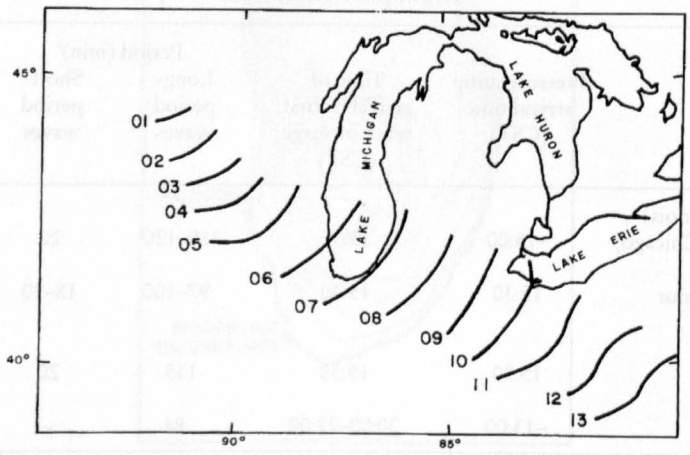

Fig. 4.9: Isochrones of the pressure jumpline of June 26, 1954, over Lake Michigan and surroundings. Numbers represent hours Central Standard Time. (PLATZMAN, 1958a)

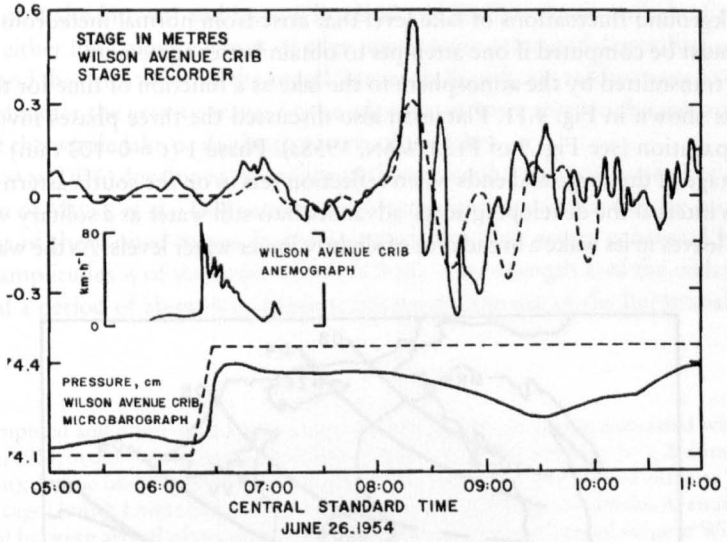

Fig. 4.10: Lake level, wind and atmospheric pressure records at Wilson Avenue crib on June 26, 1954. The broken curve of lake level shows the results of numerical computation for a squall line speed of 100 km. h-'; the broken curve of pressure gives the corresponding pressure increase assumed in the calculation. (PLATZMAN, 1958a)

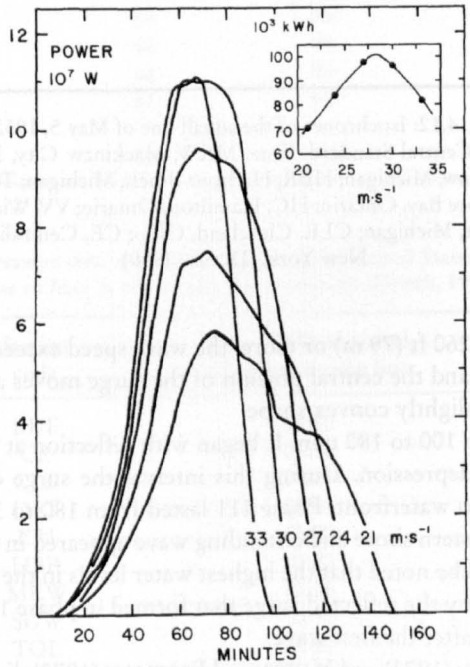

Fig. 4.11: The power transmitted by the atmosphere to the lake as a function of time for each of the five computed cases. Inset shows the total energy absorbed by the lake as a function of a squall line speed. (PLATZMAN, 1958a)

4) The background fluctuations of lake level that arise from normal meteorological disturbances must be computed if one attempts to obtain better agreement.

The power transmitted by the atmosphere to the lake as a function of time for the five cases computed is shown in Fig. 4.11. Platzman also discussed the three phases involved in this surge's propagation (see Fig. 9 of PLATZMAN, 1958a). Phase 1 (t = 0–100 min) includes the formative stage of the surge and ends when reflection sets in on the southeastern shore of the lake. In this interval the developing surge advances into still water as a solitary wave (of elevation) and leaves in its wake a broad area of slightly lower water levels. As the wave advances

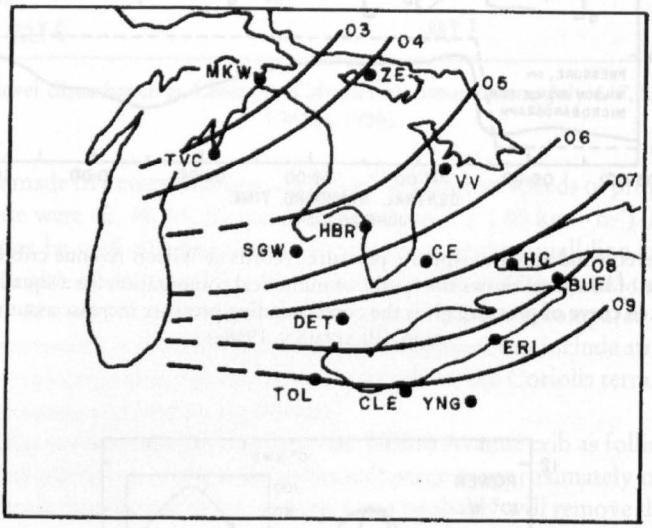

Fig. 4.12: Isochrones of the squall line of May 5, 1952.
Numbers represent hours Central Standard Time. MKW, Mackinaw City, Michigan; TVC, Traverse City, Michigan; SGW, Saginaw, Michigan; HBR, Harbour Beach, Michigan; TOL, Toledo, Ohio; YNG, Youngstown, Ohio; ZE, Gore Bay, Ontario; HC, Hamilton, Ontario; VV, Wiarton, Ontario; ERI, Erie, Pennsylvania; DET, Detroit, Michigan; CLE, Cleveland, Ohio; CE, Centralia, Ontalio; BUF, Buffalo, New York. (DONN, 1959)

into depths greater than 260 ft (79 m) or more, the wave speed exceeds the squall line speed (54 knots [100 km. h-']) and the central portion of the surge moves ahead of the squall line and the surge assumes a slightly convex shape.

Phase 11 lasted from 100 to 180 min. It began with reflection at the southeastern shore followed by a wave of depression. During this interval the surge contracted and moved southwest to the Chicago waterfront. Phase 111 lasted from 180 to 300 min. It began with reflection at the southwestern shore and a standing wave appeared in the southernmost portion of the lake. It should be noted that the highest water levels in the Chicago area were not produced in phase 1 but by the reflected surge that formed in phase 11 and arrived from the north-east about 85 min after the first wave.

FREEMAN and MURTY (1972) and MURTY and FREEMAN (1973) discussed a squall line generated surge on Lake Huron. This will be discussed in section 7. 1. DONN (1959) studied the storm surges in Lakes Huron and Erie due to a squall line on May 5, 1952. The travel time curves of the squall line are shown in Fig. 4.6. The pressure and wind data are summarised in Tables 4.6 and 4.7, respectively. Water level data are used from MacKinaw City and Harbour

Beach (both on Lake Huron) and from Cleveland and Buffalo (both on Lake Erie). DONN showed that either long gravity waves or edge waves were generated depending on the local topography and the orientation of the squall line track. Significant seiches were excited when the periods of either the gravity waves or the edge waves were close to the natural modes of oscillation of the whole lake or distinctive parts of the lake.

GREENSPAN (1956) developed an analytical theory for the transient aspects of the steady-state problem of MUNK et al. (1956) and applied it to edge wave generation by hurricanes on the east coast of the United States. It was assumed that edge waves generated here in this fashion had amplitudes η of the order of 3 ft (0.9 m), a wavelength λ of the order of 200 mi (322 km), and a period of about 6 h. These scales permit the use of the linear shallow-water theory.

Table 4.5: Computed and observed time intervals between significant events associated with the squall line of June 26, 1954, in the United States. Columns: 1, speed of squall line (km – h-'); 2, duration of pressure jump (min); 3, time interval between first surge at Michigan City and second surge at Wilson Avenue Crib (Chicago) (min); 4, time interval between first and second surges at Wilson Avenue Crib (min); 5, time interval between arrival of pressure jump and occurrence of and second surge at Wilson Avenue Crib (min); 6, time interval between second surge and first one following depression at Wilson Avenue Crib (min). (PLATZMAN, 1958a)

1	2	3	4	5	6
			Computed		
78	14.3	55	85	109	35
89	12.5	63	85	114	25
100	11.1	66	85	118	20
111	10.0	68	85	121	18
122	9.1	67	85	121	18
			Observed		
	5	68	88	113	6

Table 4.6: Atmospheric pressure data at several stations in the United States and Canada for the squall line of May 5, 1952 (NA, not available). (DONN, 1959)

Location	Station code	Time (EST) of arrival of pressure jump line	Magnitude of pressure jump (mb)
Buffalo, NY	BUF	08:00	4.06
Centralia, Ont.	CE	06:30	5.08
Cleveland, OH	CLE	09:28	2.71
Detroit, MI	DET	07:38	2.37
Erie, PA	ERI	08:00	3.39
Harbour Beach,	HBR	05:20	NA
Mackinaw City, MI	MKW	02:36	NA
Saginaw, MI	SGW	05:40	2.03
Toledo, OH	TOL	09:40	0.68
Traverse City, MI	TVC	03:45	0.68
Youngstown, OH	YNG	09:30	3.39
Gore Bay, Ont.	ZE	04:30	3.39
Hamilton, Ont.	HE	07:30	NA
Wiarton, Ont.	VV	05:15	4.74

The equations of motion and continuity are in the usual notation:

$$\frac{\partial u}{\partial t} = -\frac{1}{\rho}\frac{\partial \rho}{\partial x}$$

$$\frac{\partial v}{\partial t} = -\frac{1}{\rho}\frac{\partial \rho}{\partial y} \qquad (4.4)$$

Table 4.7: Wind data at several stations in the United States and Canada for the squall line of May 5, 1952. (DONN, 1959)

Station	Wind data
Buffalo, NY	On arrival of pressure jump, weak winds shifted from east to north
Cleveland, OH	On arrival of pressure jump, winds at 32 km. h-' from north-east shifted to 48 km. h-' from south-east
Detroit, MI	On arrival of pressure jump, winds at 40 km. h-' from south east shifted to 63 km. h-' from north-east
Erie, PA	Winds of 35 km. h-' from the north. On arrival of pressure jump, winds shifted to south-east
Mackinaw City, MI	Winds of 58 km. h-' shifted at 02:36 (EST)
South Bend, IN	Winds of 29 km. h-' from northwest. On arrival of jump, wind shifted to north-east to north-north-east
Toledo, OH	On arrival of jump, wind shifted from south to north (19–24 km.h-1)
Tranverse City, MI	On arrival of jump, wind shifted from south-east to east (32–40 km. h-')
Youngstown, OH	On arrival of jump, wind shifted from north to southeast. (48–56 km. h-')
Centralia, Ont	On arrival of jump, wind shifted from south-south-west to north-north-east
Gore Bay, Ont.	Wind shifted from east to north (16–41 km. h-')
Hamilton, Ont.	Wind from northeast at 16 km/h-'.
Wiarton, Ont	Wind speed increased from 5 to 27 km. h-' and shifted from north-east to north-north-east

The computed and observed edge wave periods and duration for four hurricanes are compared in Table 4.2.

REDFIELD and MILLER (1957) divided hurricane-produced surges into three parts: the forerunner, the hurricane surge, and resurgence. The forerunner is a slow and gradual change in the water level, commencing several hours before the arrival of the storm. There appears to be good coherence between the records at nearby stations in this stage, and one must consider winds over a more extended region than the hurricane proper. Facing the coast from the ocean, if the hurricane moves to the right along the coast, the forerunner usually is a rise in the water level and if the hurricane moves to the left, the forerunner consists of a decrease in the water level.

The hurricane surge is a sharp rise in the water level that occurs at about the time the hurricane center passes over the station. The duration of this stage usually does not exceed 2.5-5 h. In this stage, the coherence between neighbouring stations is not good. This means that the strong winds in the hurricane proper are responsible for the water level oscillations. In the Northern Hemisphere, the highest water levels occur to the right of the hurricane track.

The resurgence, being unexpected (since the storm has passed), could be dangerous. These were attributed by MUNK et al. (1956) to a wake of waves in the trail of the hurricane, and these have periods of free edge waves. KAJIURA (1959) mentioned that even at stations close by (i.e. separated only by one wavelength) the periods could be considerably different. He attributed the resurgence to a free onshore-offshore standing wave on the shelf.

WEBB (1976) considered resonance problems of long gravity waves on the continental shelf. He began with a simple model of a rectangular continental shelf at the end of a canal. It is assumed that a Kelvin wave propagates along the canal, which is partly absorbed and partly reflected by the continental shelf. The depth of the canal is of the same order as that of the deep oceans and the shelf parameters are taken to represent the Patagonian Shelf off Argentina. The simple analytical model showed that usually most of the incident wave energy is reflected by the edge of the shelf. However, at the dominant shelf resonance frequencies, more than 95% of the energy is absorbed by the shelf.

4.3 Interaction between Storm Surges and Tides

The traditional method of subtracting the astronomical tide from the observed water level and treating the residue as storm surge assumes that tide and surge are linearly additive and that there is no non-linear interaction. However, observations show that there are situations in which there is an interaction (i.e. tide influencing the propagation of the surge and vice-versa), especially in shallow areas. The interaction phenomenon, although probably present in other water bodies as well, appears to be quite pronounced in the Thames Estuary of the North Sea. In a series of papers, PROUDMAN (1955a, 1955b, 1957, 1958) studied this problem analytically.

4.3.1 Numerical Models of Tide-Surge Interaction in the Bay of Bengal

FLIERL and ROBINSON (1972) have documented many cases where the occurrence of abnormally high sea-surface level in the Bay of the Bengal has led to coastal flooding and inundation. The genesis of these events is to be found in the combined effect of the astronomical tide and a surge generated by a tropical cyclone. The principle component is the surge but, depending on the relative phase of the two processes, the sea-surface elevation may either be increased above, or decreased below its pure surge value. The mutual interaction is, however, nonlinear and the dynamics of both processes must be considered simultaneously.

Many analyses of surge generation by hurricanes, typhoons and tropical cyclones have now been made. Particular mention is made here of the numerical modelling of these phenomena by JELESNIANSKI (1965, 1966, 1967), MIYAZAKI et al. (1961), DAS et al. (1974) and SINHA et al. (1996). More recently, JOHNS et al. (1981, 1982, 1983 a, b) have developed several numerical models for application along the east coast of India. A fully nonlinear model to

analyse tide-surge interaction in the Bay of Bengal has been described and applied to the coastal waters off Bangladesh by JOHNS and ALI (1980), JOHNS et al. (1985), ROY (1995, 1999 a, 1999 b), ALI et al. (1997a, b) and ALI (1980c), DAS (1980), HENRY et. al (1997).

The general procedure followed in the modelling of tide-surge interaction is to begin by generating the co-oscillating tide in a semi-enclosed basin by prescribing the temporal variation of the sea-surface elevation along the open boundary. The value of this is supposed known from observations of the tidal state in the adjacent ocean. The pure tidal solution developed in the basin then provides the initial dynamical conditions for the storm surge simulation with tidal forcing along the open-sea boundary continuing during the integration. This method has been successfully applied in studies of the tide-surge interaction in the North Sea (see, for example, BANKS, 1974) but its practical application in the Bay of Bengal is hampered by the absence of adequate tidal data along the boundary separating the Bay from the northern Indian Ocean.

DAS (1980) used a nonlinear model to study the tide-surge interaction in the Meghna estuary. ALI (1980c) stated that about one third of the area of Bangladesh is penetrated by tide (through estuaries and rivers). Maximum tidal range (up to 6.1 m) and surge are found in the Meghna estuary.

Tide-surge interaction during the November 1970 Chittagong cyclone is shown in Fig. 4.13–4.15. It may be seen that at Patenga, maximum surge occurred at time of high tide whereas at Amatali the peak surge occurred after the occurrence of high tide. However, at Kaikhali the peak water level elevation is smaller than due to the tide alone. ALI (1980c) ascribed this to the effect of the offshore wind component, which drives the water from the rivers located to the west of the cyclonic track. The two small peaks in the total elevation near the time of high tide are probably due to the tide-surge interaction.

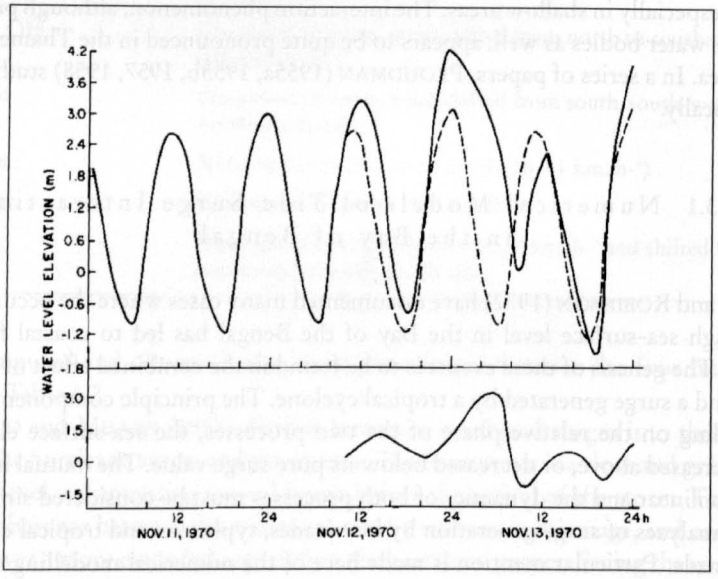

Fig. 4.13: Water level at Patenga, Bangladesh, during November 11–13, 1970. Top: Observed water level (tide + surge) is shown by the solid line and the computed water level by the broken line; bottom: observed storm surge. (ALI, 1980c)

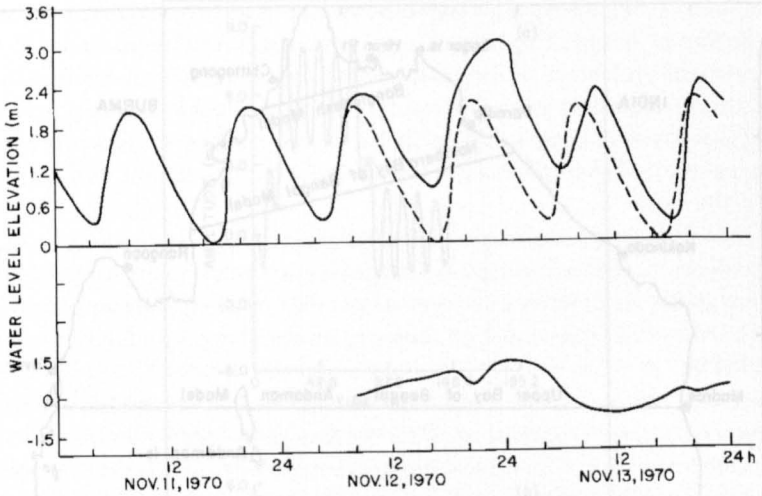

Fig. 4.14: Water level at Amtali, Bangladesh, during November 11–13, 1970. Refer to Fig. 4.13 for explanation. (ALI, 1980c)

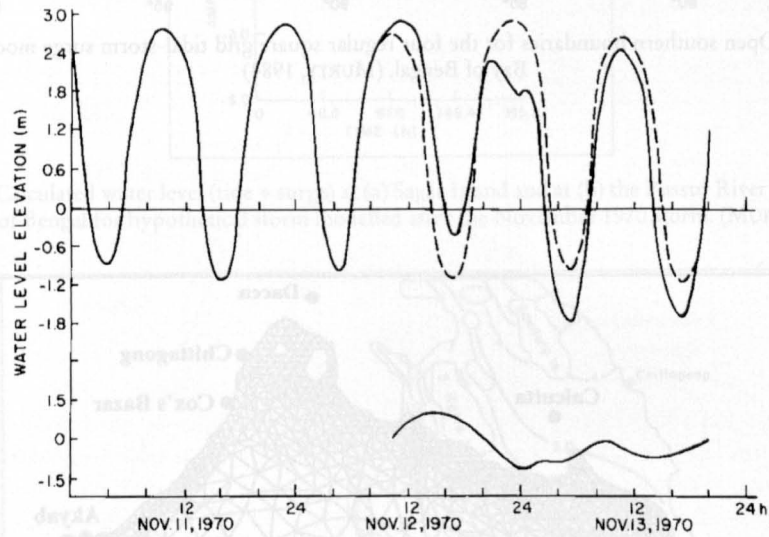

Fig. 4.15: Water level at Kaikhali, Bangladesh during November 11–13, 1970. Refer to Fig. 4.13 for explanation. (ALI, 1980c)

MURTY and HENRY (1983) and HENRY and MURTY (1982) developed a series of numerical models for tides and surges in the Bay of Bengal. The regions covered by the various regular grid models are shown in Fig. 4.16. The irregular triangular grid that has also been used is shown in Fig. 4.17. The computed water level (tide + surge) at Sagar Island and the Pussur River entrance is shown in Fig. 4.18. The contours of the computed surge are shown in Fig. 4.19.

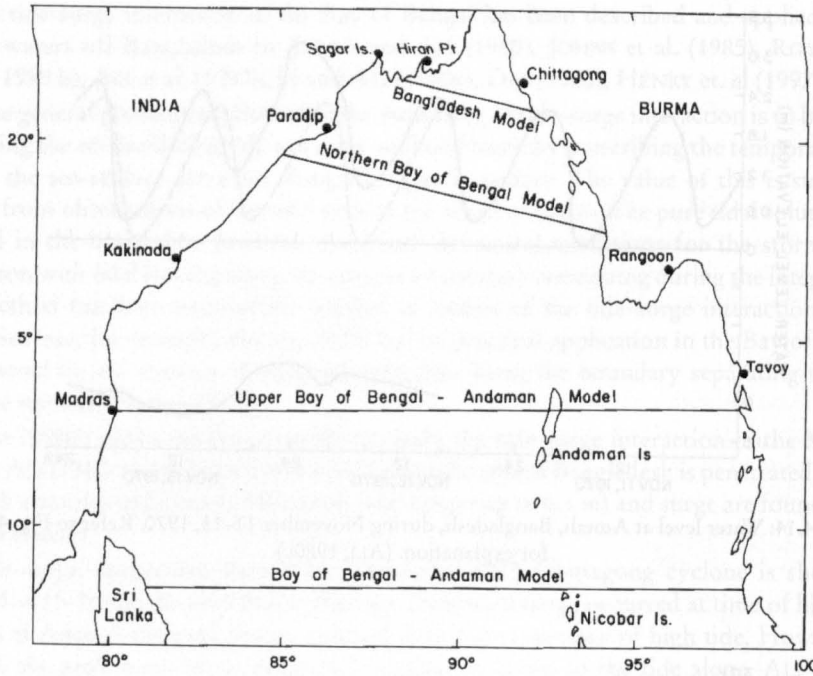

Fig. 4.16: Open southern boundaries for the four regular square grid tidal-storm surge models for the Bay of Bengal. (MURTY, 1984)

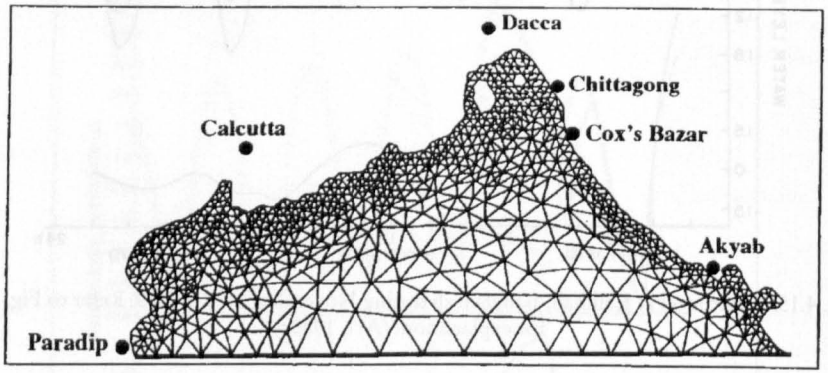

Fig. 4.17: Irregular triangular grid model for tides and storm surges in the northern part of the Bay of Bengal. (MURTY, 1984)

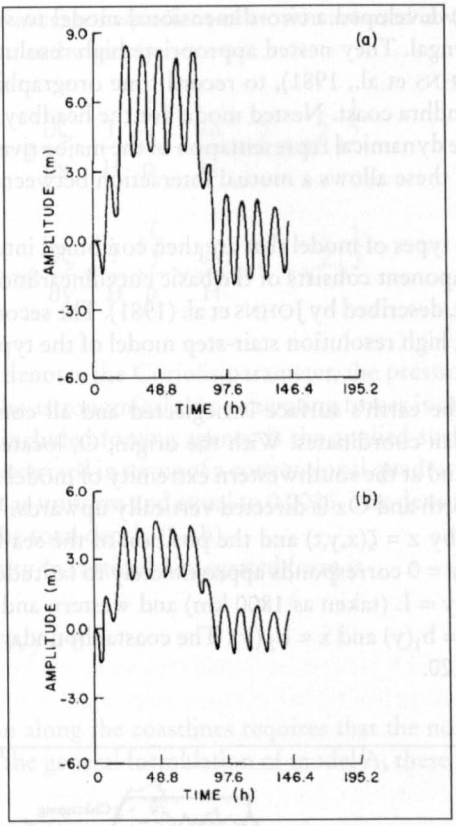

Fig. 4.18: Calculated water level (tide + surge) at (a) Sagar Island and at (b) the Pussur River entrance in the Bay of Bengal for hypothetical storm modelled after the November 1970 storm. (MURTY, 1984)

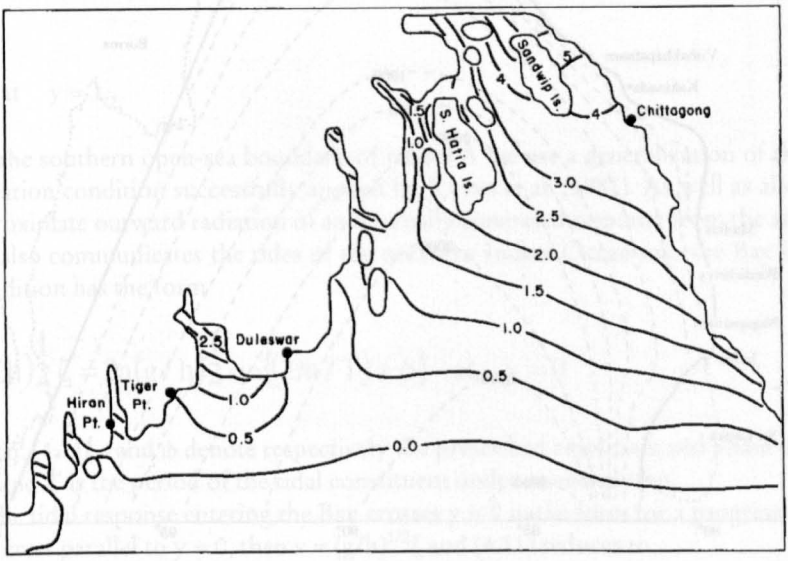

Fig. 4.19: Storm surge heights in the northern part of the Bay of Bengal from the hypothetical storm modelled after the November 1970 storm. (MURTY, 1984)

JOHNS et al. (1985) developed a two-dimensional model to study the tide-surge interaction in the Bay of Bengal. They nested appropriate high resolution models in their basic storm surge model (JOHNS et al., 1981), to record time orographical detail in the headbay region and along the Andhra coast. Nested model for the headbay region is particularly important as it includes the dynamical representation of the major rivers comprising the Ganges Delta. The inclusion of these allows a mutual interaction between the dynamics in the Bay and those in the Delta.

They consider two types of model that are then combined into a unified computational scheme. The major component consists of the basic curvilinear model for the Bay of Bengal (referred to as model A), described by JOHNS et al. (1981). The second component is a nested, and more conventional, high resolution stair-step model of the type described, for example, by HEAPS (1969).

The curvature of the earth's surface is neglected and all conditions are referred to a system of plane Cartesian coordinates. With the origin, O, located within the equilibrium level of the sea-surface and at the southwestern extremity of model A, Ox points towards the east, Oy towards the north and Oz is directed vertically upwards. The displaced position of the sea surface is given by $z = \zeta(x,y,t)$ and the position of the sea floor by $z = -h(x,y)$. An open / sea boundary at $y = 0$ corresponds approximately to latitude 6°N. A northern coastal boundary is situated at $y = L$ (taken as 1800 km) and western and eastern coastlines correspond respectively to $x = b_1(y)$ and $x = b_2(y)$. The coastal boundary configuration in model A is delineated in Fig. 4.20.

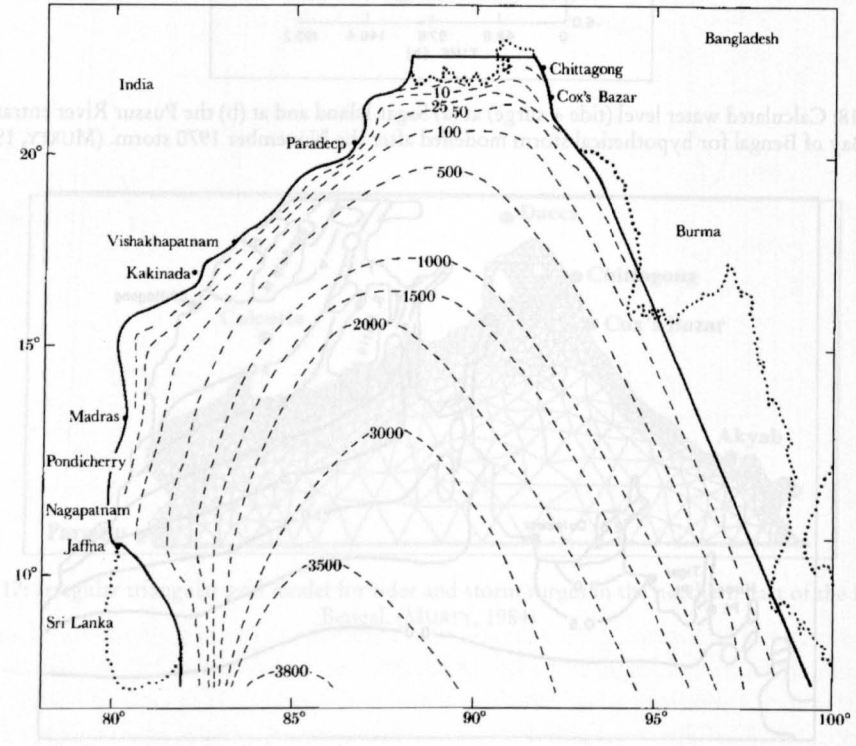

Fig. 4.20: The coastal configuration in model A and the isobaths of the model bathymetry. The numbers refer to depth in meters. (JOHNS et al., 1985)

Conventional depth-averaged equations of motion are used in which the depth-averaged components of velocity, u and v satisfy

$$\frac{\partial u}{\partial t}+u\frac{\partial u}{\partial x}+v\frac{\partial u}{\partial y}-fv=-g\frac{\partial \zeta}{\partial x}-\frac{1}{H}\frac{\tau_x^{\zeta}}{\rho}-\frac{ku}{H}(u^2+v^2)^{\frac{1}{2}} \tag{4.5}$$

$$\frac{\partial v}{\partial t}+u\frac{\partial v}{\partial x}+v\frac{\partial v}{\partial y}-fu=-g\frac{\partial \zeta}{\partial y}+\frac{1}{H}\frac{\tau_y^{\zeta}}{\rho}-\frac{kv}{H}(u^2+v^2)^{\frac{1}{2}} \tag{4.6}$$

In (4.5) and (4.6), f denotes the Coriolis parameter, the pressure is taken as hydrostatic and the direct effect of the astronomical tide-generating forces is omitted.

The sole explicitly included forcing agency is the applied surface wind stress (τ^{ζ}_x, τ^{ζ}_y). Bottom friction is parameterized in terms of a conventional quadratic stress law with the friction coefficient, k, taken as uniform and equal to 0.0026. The density of the water, ρ, is assumed uniform and H is the total depth, (ζ + h).
The equation of continuity in vertically integrated form is

$$\frac{\partial \zeta}{\partial t}+\frac{\partial}{\partial x}(Hu)+\frac{\partial}{\partial y}(Hv)=0 \tag{4.7}$$

Boundary condition along the coastlines requires that the normal component of velocity is zero. In terms of the general formulation of model A, these lead to

$$u-vb_1'(y)=0 \quad \text{at} \quad x=b_1(y), \tag{4.8}$$

$$v-vb_2'(y)=0 \quad \text{at} \quad x=b_2(y), \tag{4.9}$$

and

$$v=0 \quad \text{at} \quad y=L, \tag{4.10}$$

At the southern open-sea boundary of model A we use a generalization of the linearized radiation condition successfully applied by JOHNS et al. (1981). As well as allowing for the approximate outward radiation of an internally generated response from the analysis region, it also communicates the tides of the northern Indian Ocean into the Bay of Bengal. The condition has the form

$$v+(g/h)^{\frac{1}{2}}\zeta=2a(g/h)^{\frac{1}{2}}\sin\{(2\pi t/T)+\phi\} \quad \text{at} \quad y=0 \tag{4.11}$$

In eq. (4.11) a and ϕ denote respectively the prescribed amplitude and phase of the tidal forcing and T is the period of the tidal constituent under consideration.

If the tidal response entering the Bay crosses y = 0 in the form for a progressive wave with its crest parallel to y = 0, then $v = (g/h)^{1/2}\zeta$ and (4.11) reduces to

$$\zeta = a\sin\{(2\pi t/T)+\phi\} \quad \text{at} \quad y=0 \tag{4.12}$$

In this case, a and ϕ correspond to the amplitude and phase of the tidal elevation along $y = 0$. A consequence of applying (4.11) rather than (4.12) is that the values of neither ζ nor v are separately prescribed along the open-sea boundary of model A. Thus, during the solution process, the boundary values of both ζ and v may correlatively adjust subject only to (4.11). We anticipate that such a solution procedure, which is based on prescribing conditions on an incoming characteristics will be superior to one using (4.12), especially if $y = 0$ should coincide with a nodal line. Further generalization of (4.11) to a discrete spectrum of tidal constituents follows without difficulty.

High resolution stair-step models are nested within model A so as to represent more fully the orographical detail of the headbay region and the Andhra coast of India. For the headbay, the nested model is referred to as model B and the stair-step boundary configuration is delineated Fig. 4.21. In contrast with the parent model A, the northern boundary of model B does not consist of a continuous vertical wall. Instead, one-dimensional dynamical models have been included to represent some of the rivers entering the head of the Bay of Bengal. The southernmost limit of model B consists of an open-sea boundary along latitude 19° 33' N where elevation values are prescribed. These are determined from the response in model A. An important feature of the scheme is that the response in model A is independent of that in model B. On the other hand, the response in model B is dependent on that generated in model A. Indeed, we find that the results from model A become increasingly unrealistic in the region of the Ganges Delta owing to the omission of any representation of the complex river system. Model B is superior in this respect as the representation of the rivers, although crude, avoids a complete refection of the response at $y = L$ and the local development of unrealistically high sea-surface elevations.

In model B, east-west separation distance between points at which the elevation is compute is approximately 17.6 km. The north-south distance between computational points is approximately 19.8 km. The grid-point arrangement is staggered in such a way that ζ is computed at the centre of a grid cell while u and v are computed at the mid-points of its y-directed and x-directed sides respectively. The vanishing of the normal component of velocity at a coastline is then readily achieved by an appropriate stair-step representation of the boundary.

Conditions in each of the rivers satisfy equations of the form.

$$\frac{\partial v}{\partial t} + v\frac{\partial v}{\partial y} = -g\frac{\partial \zeta}{\partial y} - \frac{kv|v|}{H} \tag{4.13}$$

and

$$b\frac{\partial \zeta}{\partial t} + \frac{\partial}{\partial y}(bHv) = 0 \tag{4.14}$$

Thus, in the dynamical equation (4.13), we omit the effect of wind-stress forcing in the rivers. At the point of entry into model B, the elevation and momentum flux are made continuous. In the continuity equation (4.14), b denotes the local breadth of the river. At the river's point of communication with model B, the mass flux is made continuous. Juncture conditions of a similar kind have been described by JOHNS and ALI (1980). It is noteworthy that the resulting interaction between the rivers and model B is two-way because the dynamical response in either may affect that in the order.

Each of the rivers is taken to have a length of 200 km with no mass flux of water through its head. Each river has a uniform breadth of 18 km except the Meghna (in the extreme east),

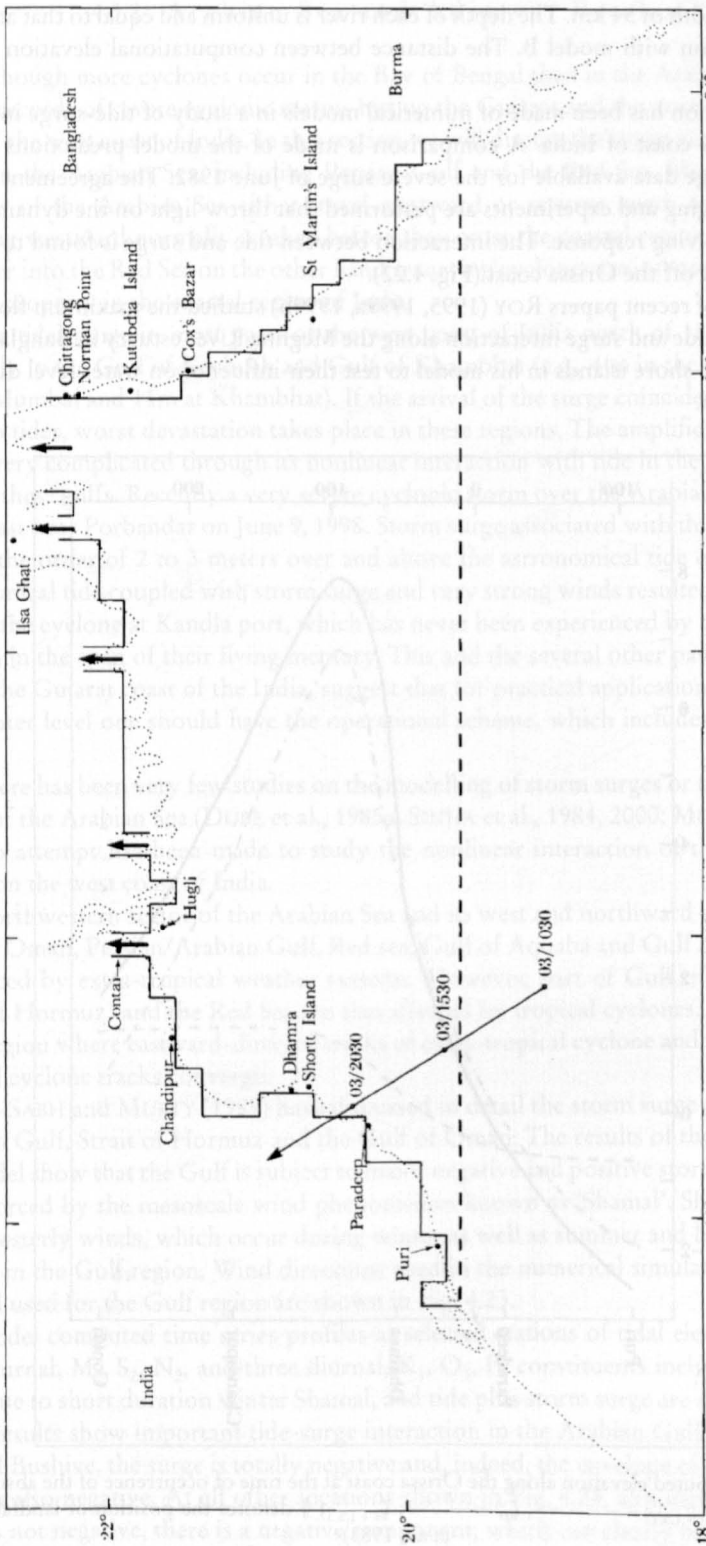

Fig. 4.21: The coastal configuration in model B and the idealized track of the Orissa cyclone. The numbers on the track refer to the times (IST) at which the centre of the cyclone passed through the marked positions on 3 June 1982. (JOHNS et al., 1985)

which has a breadth of 54 km. The depth of each river is uniform and equal to that at its point of communication with model B. The distance between computational elevation points is taken as 20 km.

An application has been made of numerical models in a study of tide-surge interaction along the Orissa coast of India. A comparison is made of the model predictions with the limited tide-gauge data available for the severe surge of June 1982. The agreement between these is encouraging and experiments are performed that throw light on the dynamical character of the evolving response. The interaction between tide and surge is found to lead to a substantial effect off the Orissa coast (Fig. 4.22).

In a series of recent papers ROY (1995, 1999a, 1999b) studied the maximum flood levels associated with tide and surge interaction along the Meghna River estuary in Bangladesh. He also included off-shore islands in his model to test their influence on water level due to tide surge interaction.

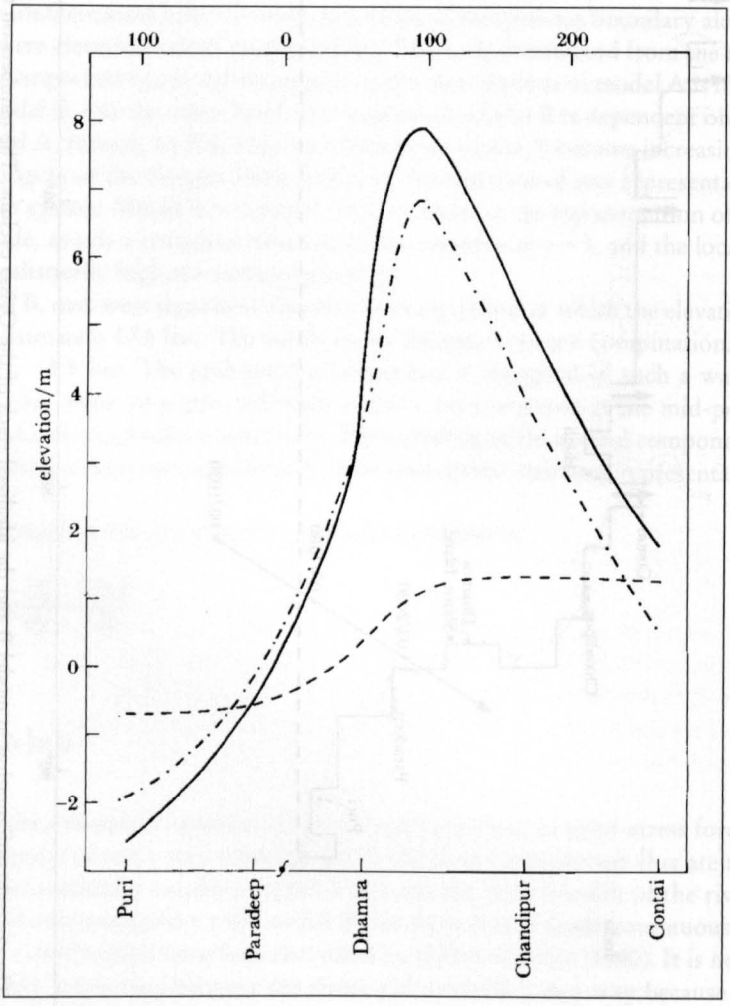

Fig. 4.22: The computed elevation along the Orissa coast at the time of occurrence of the absolute peak elevation; ___, $\zeta_{s+t+I.S.T}$; - - - - - -, ζ_t; —— . —, $\zeta_{s+I.S.T}$; § denotes the position of landfall. (JOHNS et al., 1985)

4.3.2 Arabian Sea and Adjacent Persian Gulf

Although more cyclones occur in the Bay of Bengal than in the Arabian Sea, there are several records of severe cyclonic storms hitting the Gujarat and the north Maharashtra regions of the west coast of India. In this section we will discuss the storm surge and tide interaction in the Arabian Sea, including Persian Gulf and the Red Sea. Most of the tropical cyclones of the Arabian Sea either travel westward or recurve north eastward, cyclones travelling westward normally weaken before they cross the coastal regions of Saudi Arabia and enter into the Red Sea on the other hand recurving cyclones are intense and cause loss of life and property in the coastal region of India.

The tidal range in most parts of the west coast of India north of 18° N is quite large especially in the Gulf of Kachchh and Gulf of Khambhat (e.g., 4 m in the Gulf of Kachchh, 8 m at Mumbai and 11m at Khambhat). If the arrival of the surge coincides with the time of the high tides, worst devastation takes place in these regions. The amplification of surge becomes very complicated through its nonlinear interaction with tide in the shallow water region of these gulfs. Recently a very severe cyclonic storm over the Arabian Sea crossed Gujarat coast near Porbandar on June 9, 1998. Storm surge associated with this tropical cyclone was of the order of 2 to 3 meters over and above the astronomical tide of 6.6 meters. The astronomical tide coupled with storm surge and very strong winds resulted in a phenomenal fury of the cyclone at Kandla port, which has never been experienced by the community of the area in the span of their living memory. This and the several other past cyclones, which struck the Gujarat coast of the India, suggest that for practical application of predicting the total water level one should have the operational scheme, which includes tide-surge interaction.

There has been very few studies on the modelling of storm surges or tides in the eastern sector of the Arabian Sea (DUBE et al., 1985a; SINHA et al., 1984, 2000; MITRA, 1990). However, no attempt has been made to study the nonlinear interaction of the tide and storm surges on the west coast of India.

Northwestern sector of the Arabian Sea and its west and northward extension through Gulf of Oman, Persian/Arabian Gulf, Red sea, Gulf of Aquaba and Gulf of Suez are mainly influenced by extra-tropical weather systems. However, part of Gulf of Oman (South of Strait of Hormuz) and the Red Sea are also affected by tropical cyclones. Strait of Hormuz is the region where eastward-directed tracks of extra-tropical cyclone and westward moving tropical cyclone tracks converge.

EL-SABH and MURTY (1989) have discussed in detail the storm surge phenomena in the Arabian Gulf, Strait of Hormuz and the Gulf of Oman. The results of their two-dimensional model show that the Gulf is subject to major negative and positive storm surges. The model is forced by the mesoscale wind phenomenon known as 'Shamal'. Shamal refers to the northwesterly winds, which occur during winter as well as summer and have significant influence in the Gulf region. Wind directions used in the numerical simulation together with the grid used for the Gulf region are shown in Fig. 4.23.

Model computed time series profiles at selected stations of tidal elevation (with three semi-diurnal, M_2, S_2, N_2, and three diurnal, K_1, O_1, P_1 constituents included), storm surge alone due to short duration winter Shamal, and tide plus storm surge are shown in Fig. 4.24. These results show important tide-surge interaction in the Arabian Gulf. At Shat-Al-Arab Bar and Bushive, the surge is totally negative and, indeed, the envelope of the tide plus surge curve is also negative. At all other locations shown in Fig. 4.24, although the predominant surge is not negative, there is a negative component, which can clearly be seen. These nega-

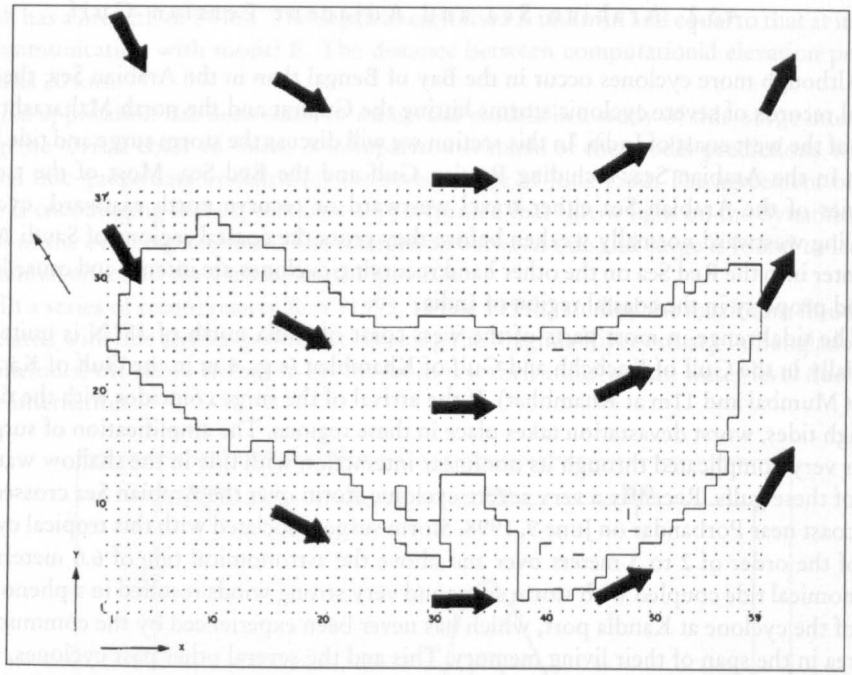

Fig. 4.23: Wind directions used in the numerical simulation. (EL-SABH and MURTY, 1989)

tive surges are due to the orientation of the storm track with reference to the topography. It may, overall, be seen that maximum amplitude of the negative surge reaches to about 3 m while maximum amplitude of positive surges is only 1m. The nature of the tide-surge interaction is different at different locations, due to the change in the tidal and surge regimes at various areas in Gulf.

4.3.3 Gulf of Suez-Red Sea System

Gulf of Suez is located in the extreme north of the Red Sea bounded by the Sinai Peninsula to the east and the Eastern Desert of the Egypt to the west (Fig. 4.25). It is connected with the Mediterranean Sea through the Suez Canal and with the Red Sea through the strait of Jubal.

Storm surges are considered to be one of the most important natural hazards that affect the Gulf and its surroundings. The analysis made by MURTY and EL-SABH (1981), based on the water levels at Port Suez for the year 1965–1966, indicated that significant surges could develop in the Gulf of Suez. On the other hand, M_2 semidiurnal tidal component dominates the tidal signal. Generally, the tidal range decreases from the entrance of the Gulf towards the bank of Tor where it reaches a very small value, and then increases again to about 1.5 m at Suez. A difference of 6 hours exists between the times of high water at the southern and northern ends of the Gulf (MORCOS, 1970). RADY et al. (1994a) used a vertically integrated two-dimensional and a five-layer three-dimensional numerical model to simulate Gulf is principal tidal component M_2. Known to be an area that is vulnerable to significant surges (MURTY and EL-SABH, 1984) and that has the largest tidal range and the shallowest water

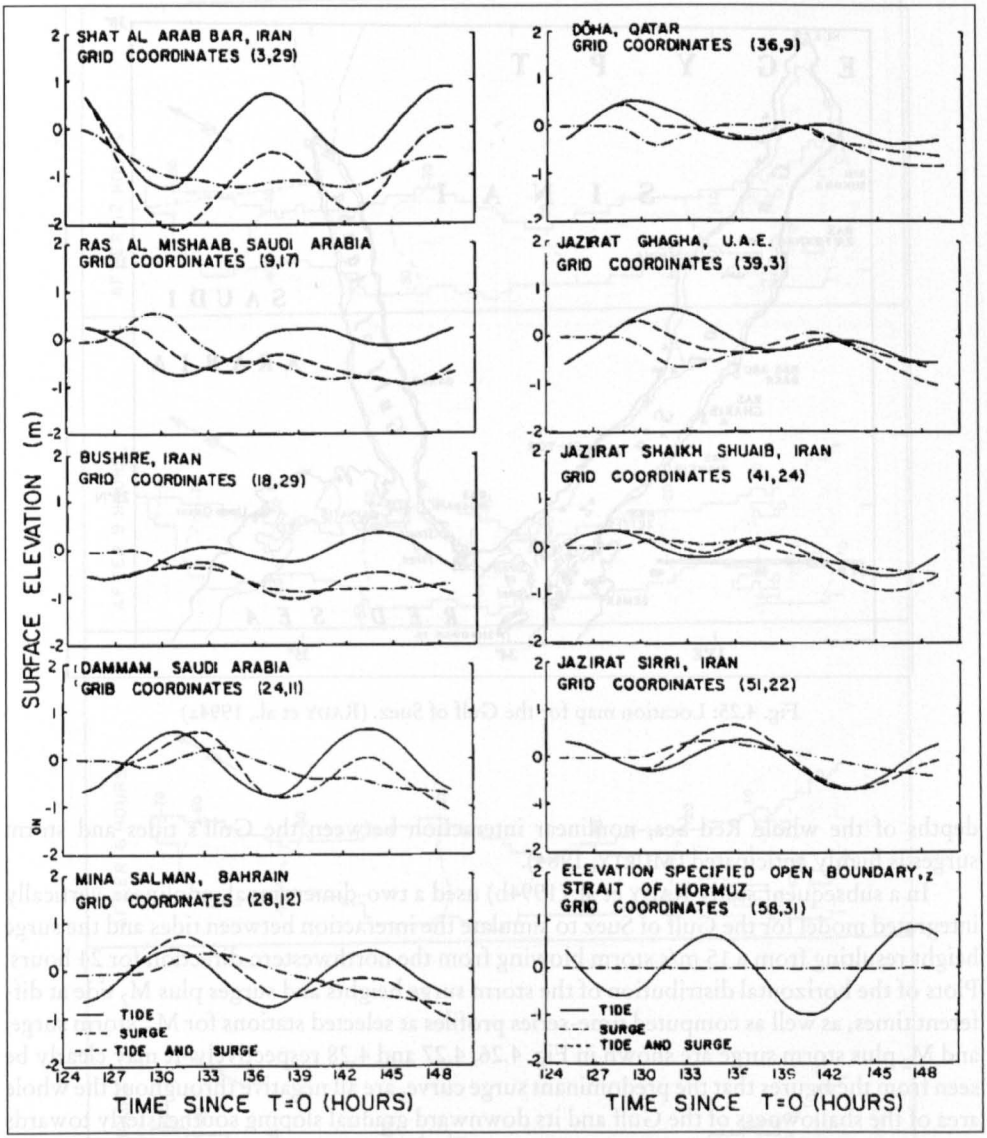

Fig. 4.24: Computed profiles of tides (including six constituents), surge only and surge plus tide at selected locations. (EL-SABH and MURTY, 1989)

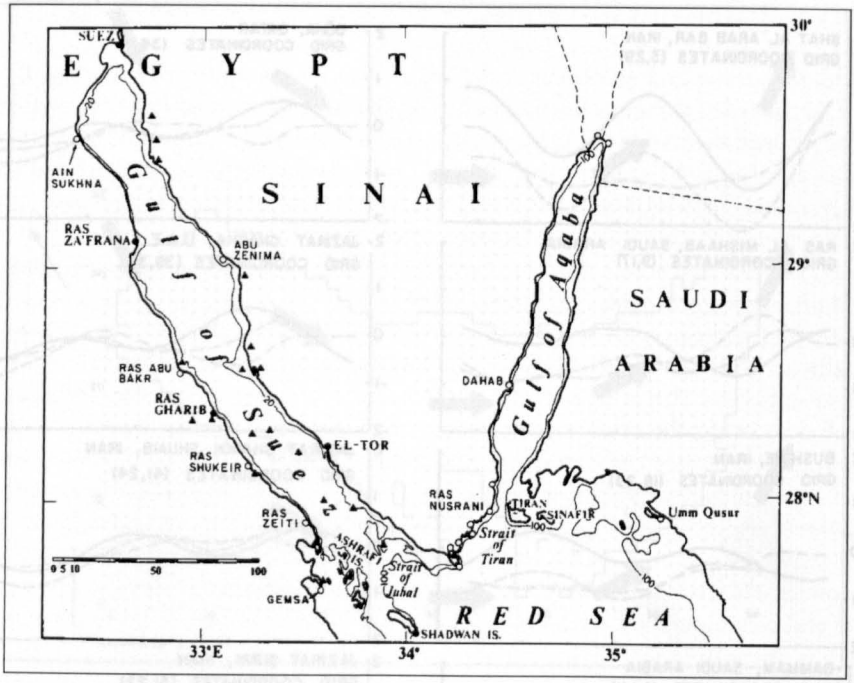

Fig. 4.25: Location map for the Gulf of Suez. (RADY et al., 1994a)

depths of the whole Red Sea, nonlinear interaction between the Gulf's tides and storm surges is highly anticipated (MURTY, 1984).

In a subsequent study RADY et al. (1994b) used a two-dimensional, nonlinear, vertically integrated model for the Gulf of Suez to simulate the interaction between tides and the surge height resulting from a 15 m/s storm blowing from the northwestern direction for 24 hours. Plots of the horizontal distribution of the storm surge heights and surges plus M_2 tide at different times, as well as computed time-series profiles at selected stations for M_2, storm surge, and M_2 plus storm surge are shown in Fig. 4.26, 4.27 and 4.28 respectively. It may clearly be seen from the figures that the predominant surge curve, are all negative throughout the whole area of the shallowness of the Gulf and its downward gradual sloping southeasterly towards the great depths of the Red Sea in the same direction of the blowing storm. Since the Gulf of Suez is part of the Red Sea system, positive surges should be expected to occur in other parts of the Red Sea. This aspect has been discussed in detail by RADY et al. (1994b).

Surge heights increase from a few centimeters at the southern end of the Gulf to over one meter in the extreme north at Suez. These heights become larger when the effect of the tide is included.

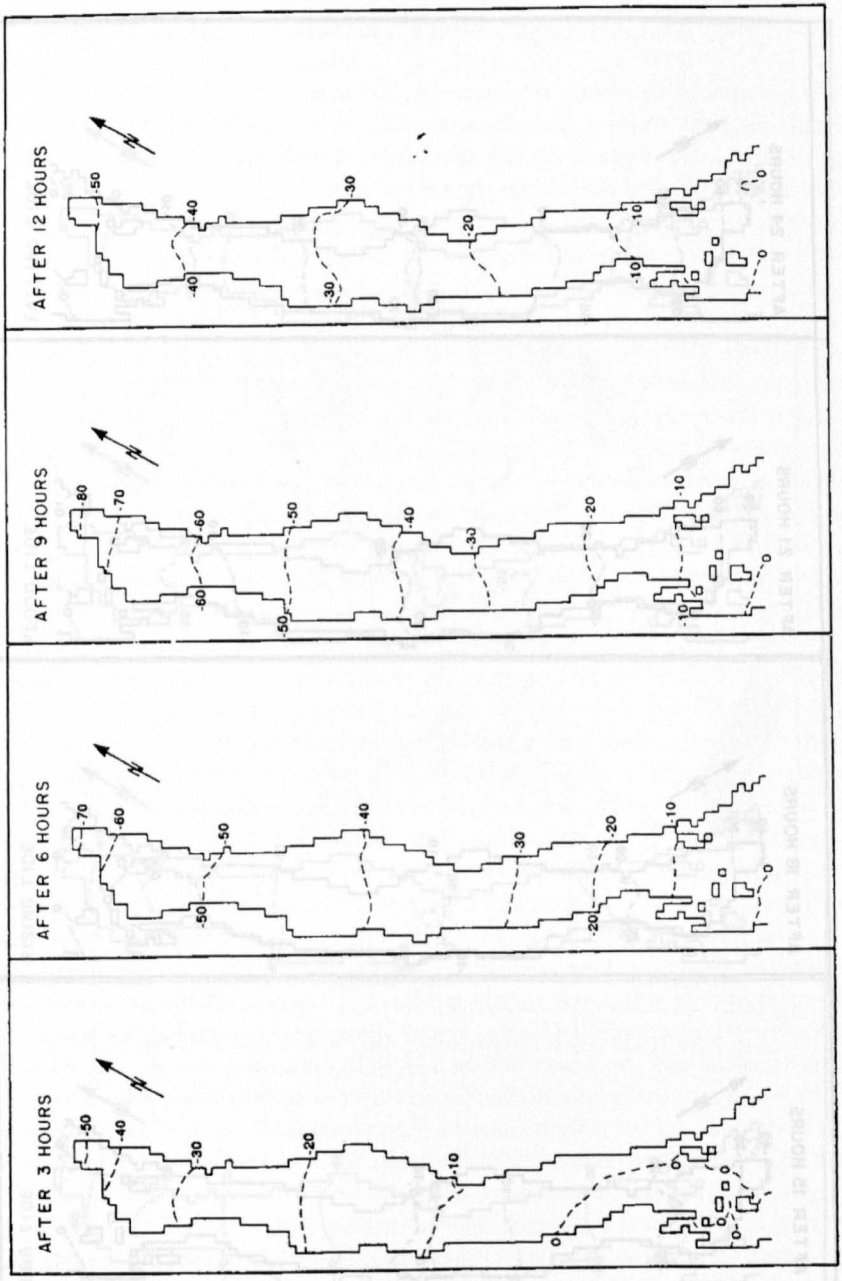

Fig. 4.26: Distribution of storm surge heights at eight different times. Elevations are in centimeters. (RADY et al., 1994 b)

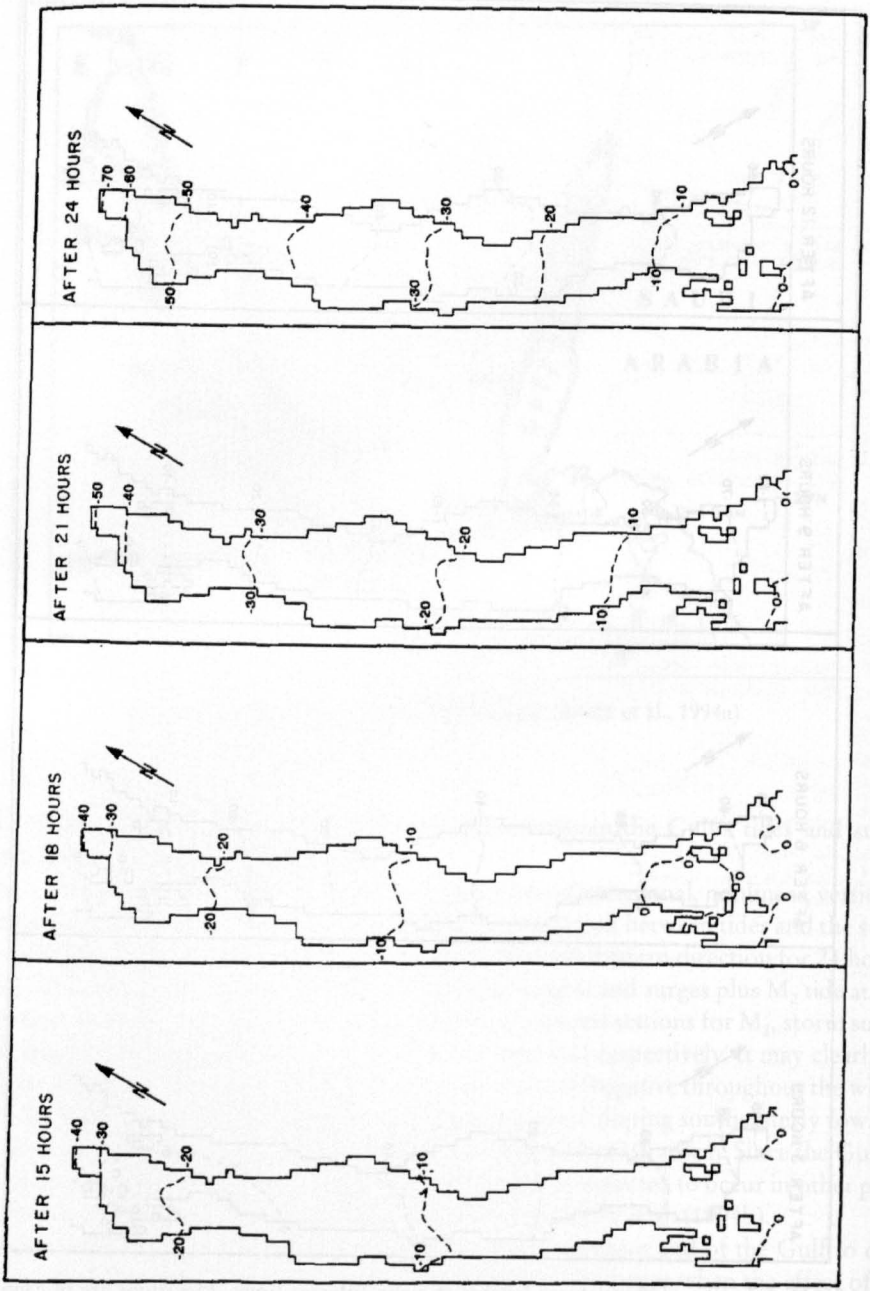

Fig. 4.27: Distribution of storm surge heights at eight different times. Elevations are in centimeters. (RADY et al., 1994 b)

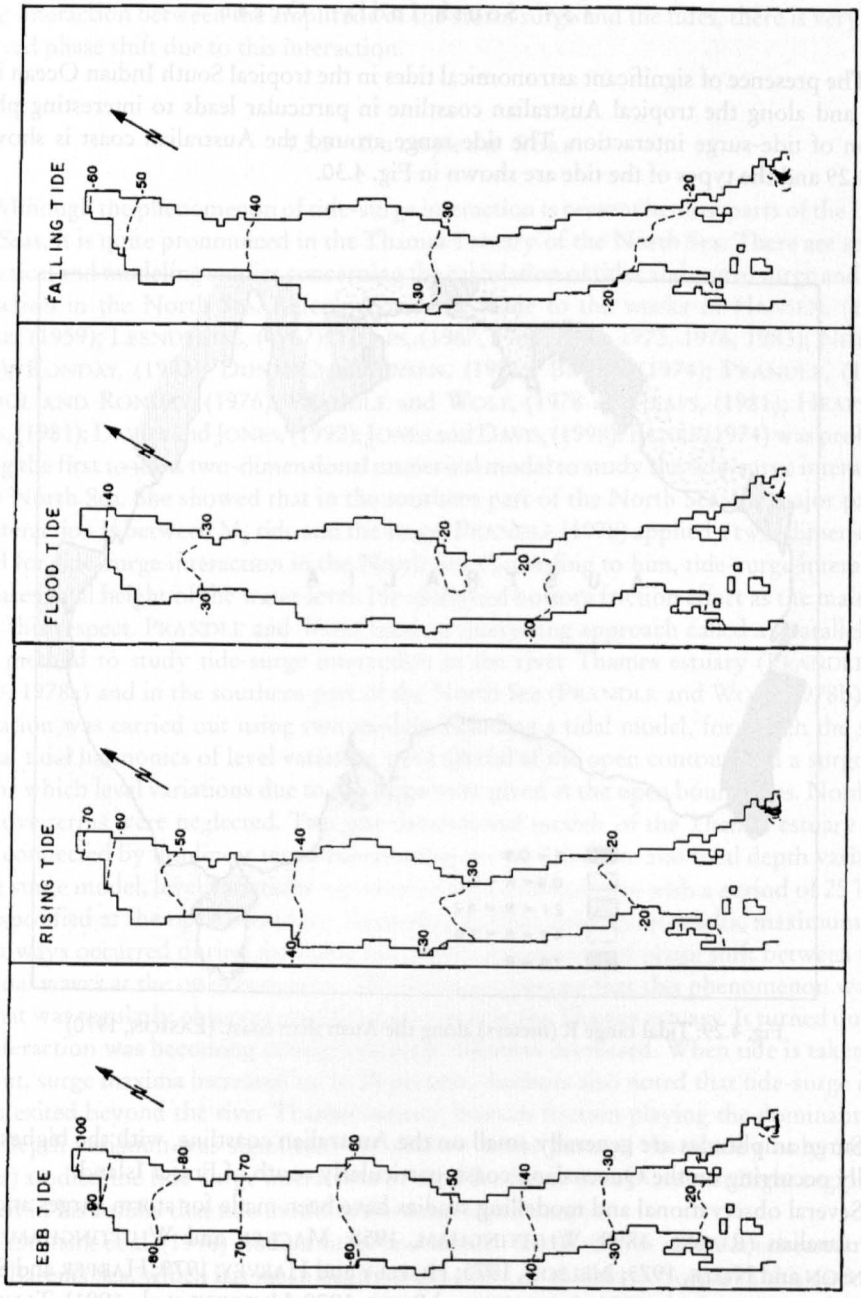

Fig. 4.28: Distribution of storm surge heights plus M_2 tide during the different stages of tide. (RADY et al., 1994 b)

4.3.4 South Indian Ocean

The presence of significant astronomical tides in the tropical South Indian Ocean in general and along the tropical Australian coastline in particular leads to interesting phenomenon of tide-surge interaction. The tide range around the Australian coast is shown in Fig. 4.29 and the types of the tide are shown in Fig. 4.30.

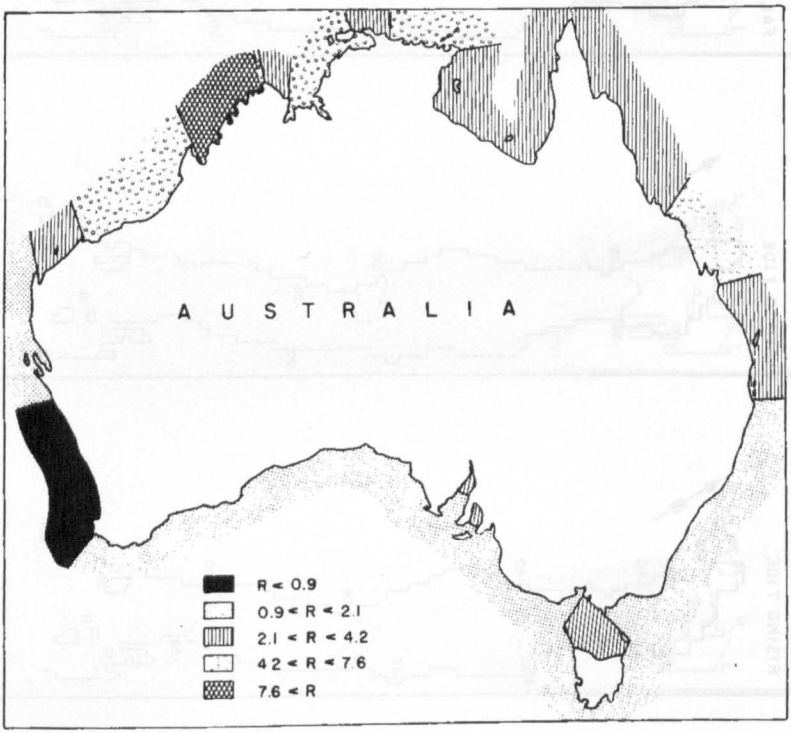

Fig. 4.29: Tidal range R (meters) along the Australian coast. (EASTON, 1970)

Surge amplitudes are generally small on the Australian coastline, with the highest level usually occurring on the Queensland coast, particularly south of Fraser Island.

Several observational and modelling studies have been made for storm surges and tides in Australian (RUSSEL, 1898; WHITTINGHAM, 1958; MACKEY and WHITTINGHAM, 1956; TRONSON and NOYE, 1973; NELSON, 1975; HOPLEY and HARVEY, 1979; HARPER and SOBEY, 1983; MIDDLETON et al., 1984; ANDREWS and BODE, 1988; HUBBERT et al., 1991). TANG et al. (1996) appear to have done the first detailed study of the tide-surge interaction for the Mackay region of the North Queensland coast. They used a two-dimensional model to simulate storm surge and tides. Their results show that with the tides included in the storm surge model the sea level elevation is generally lower than if astronomical tides are simply added to the surges. This effect is attributed by authors to the quadratic bottom friction law rather than the commonly explained reason of nonlinear interaction between the storm surge and the tides. Further, they note that although the quadratic bottom friction does cause a

strong interaction between the amplitude of the storm surge and the tides, there is very little observed phase shift due to this interaction.

4.3.5 European Seas

Although the phenomenon of tide-surge interaction is present in most parts of the European Seas, it is quite pronounced in the Thames Estuary of the North Sea. There are several theoretical and modeling studies concerning the calculation of tides and storm surge and their interaction in the North Sea. Reference may be made to the works of HANSEN, (1956); FISHER, (1959); LEENDERTSE, (1967); HEAPS, (1967, 1969, 1972, 1973, 1976, 1983); NIHOUL, (1973); RONDAY, (1973); DUNN-CHRISTENSEN, (1971), BANKS, (1974); PRANDLE, (1975); NIHOUL AND RONDAY, (1976); PRANDLE and WOLF, (1978 a); HEAPS, (1981); HEAPS and JONES, (1981); DAVIES and JONES, (1992); JONES and DAVIS, (1998). BANKS (1974) was probably among the first to use a two-dimensional numerical model to study the tide-surge interaction in the North Sea. She showed that in the southern part of the North Sea, the major part of the interaction is between M_2 tide and the surge. PRANDLE (1978) applied a two-dimensional model for tide-surge interaction in the North Sea. According to him, tide-surge interaction decreases total height of the water level. He identified bottom friction effect as the main factor in this respect. PRANDLE and WOLF used an interesting approach called a "parallel models" method to study tide-surge interaction in the river Thames estuary (PRANDLE and WOLF, 1978a) and in the southern part of the North Sea (PRANDLE and WOLF, 1978b). The simulation was carried out using two models including a tidal model, for which the semidiurnal tidal harmonics of level variation were special at the open contour, and a surge model, for which level variations due to the surge were given at the open boundaries. Nonlinear advective terms were neglected. Two one-dimensional models of the Thames estuary were used, connected by nonlinear terms representing power 2 friction and total depth variation. In the surge model, level variations represented by a sine function with a period of 25 hours were specified at the open boundary. According to their simulation results, maximum total level always occurred during the rising tide phase, irrespective of phase shift between surge and tidal waves at the open boundary. The authors supposed that this phenomenon was the one that was regularly observed during surge events in the Thames estuary. It turned out that the interaction was becoming stronger as surge duration decreased. When tide is taken into account, surge maxima increased up to 25 percent. Authors also noted that tide-surge interaction exited beyond the river Thames estuary, bottom friction playing the dominant role. Total depth variation was significant for shallow water parts of the estuary only. SIEFERT (1978a) studied the tide-surge interaction in the Elbe River in the German Bight region. He showed in his results that tide modifies the surge significantly.

VLADIMIR et al. (1996) studied surge and tides in the shelf area of the southeastern part of the Barents Sea, which has mean depth of the order of 45 meters. Surges in this region are of the same order as the tides and may even exceed them. For the model verification and for obtaining information necessary for specification of boundary conditions, results of a special observational programme in the shallow water Pechorskaya Guba were used, which provided data for the analysis of total motion and estimation of tide-surge interaction. Their results show strong nonlinear tide-surge interaction for Shvedskie Stvory where total water level decreases during rising tide period and increase during the opposite phase.

There have also been several attempts to simulate the nonlinear interaction of tides and storm surges in North Sea and Irish Sea using a three-dimensional model. It may not be pos-

sible to describe here the details of these studies. However, one may refer to the works of HEAPS, (1973, 1976, 1981); HEAPS and JONES, (1981); DAVIES and JONES, (1992, 1996); JONES and DAVIES, (1998).

4.3.6 Canada and United States

In this section we will discuss the interaction between storm surges and tides in selected water bodies in Canada and North America. The tidal range along the Canadian coast is significant. In the Bay of Funding the tidal range is more than 12 m. Along the Atlantic coast of Canada, the tide is semidiurnal and the tidal range is usually less than 2 m while the tidal range in the Gulf of St. Lawrence is less than 2.5 m. MURTY (1984) has described in detail the tidal regimes in the coastal waters of Canada and North America. In these shallow coastal waters the interaction between storm surge and tides is found to be significant.

In the St. Lawrence estuary in eastern Canada, observations indicate a predominant occurrence of positive storm surges with low tide and negative surges with high tide. MURTY and EL-SABH (1981) studied the interaction between astronomical tides and storm surges in the St. Lawrence estuary by extending simple analytical theory developed by PROUDMAN (1955a, b, 1957) for the Thames estuary. Based on PROUDMAN (1957) it can be shown that an estuary is short (with reference to long wave propagation) provided the following two conditions are satisfied

$$\left.\begin{aligned} \frac{\sigma L}{c} A &<< 1 \\ \frac{K\sigma^2 L^3 A}{hc^2} A &<< 1 \end{aligned}\right\} \qquad (4.15)$$

Where σ is the angular frequency of the tide, L is the length of the estuary, and $c = \sqrt{gh}$ The parameter A is defined as

$$A \equiv \frac{B}{2H} \qquad (4.16)$$

where, B is the tidal amplitude at the mouth. Parameter K is a coefficient of bottom friction and is taken as 0.0025. Note that it is not the physical length alone that determines whether or not an estuary is short, in the sense used by PROUDMAN.

Length L, Average depth h, and tidal amplitude B for the two portions of the St. Lawrence Estuary are summarized in Table 4.8. The values of the two PROUDMAN parameters defined by eq. (4.15) are also listed for the two sections. Based on these values, the classification into long or short estuary is made in the final column.

Table 4.8: Dimensions and classifications of the two sections of the St. Lawrence Estuary.

System	Length (km)	Average depth (cm)	Tide amplitude, B (cm)	Proudman's 1st parameter	Proudman's 2nd parameter	Classification
Sept-Iles to Saguency River	350	25×10^3	107	0.002	0.007	Short estuary
Saguency River to Quebec City	193	1800	215	0.12	6.7	Long estuary

Table 4.9: Number of occasions of positive and negative surges exceeding a given height at Tadoussac during 1965–75. Each hourly reading is treated as one occasion.

State of tide	Surge height (cm) 10	20	30	40	50	60	70	80	90	100	110	120	130	140	150	300
							(a) Positive surges									
Low	3806	1763	904	468	260	147	77	48	26	16	10	5	3	2	0	0
Rising	4195	2090	1016	515	263	129	81	61	47	29	12	8	4	3	3	3
High	4063	1843	849	390	185	96	59	33	23	14	3	2	2	2	2	2
Falling	4210	2082	1057	571	315	187	115	60	25	5	3	2	2	0	0	0
							(b) Negative surges									
Low	4466	2046	894	412	192	94	44	22	8	1	0	0	0	0	0	0
Rising	4533	2275	1146	634	324	178	94	56	35	16	5	3	2	1	0	0
High	3441	1513	710	363	205	108	52	34	19	15	13	12	9	7	4	2
Falling	4110	1934	851	385	205	102	53	35	18	12	8	7	5	3	1	0

Table 4.10: Comparison between theory and observation of the tide-surge interaction in the St. Lawrence Estuary. H, High tide; L, low tide; R, rising tide; F, falling tide; A, inagreement; D, in disagreement; N, neither agreement nor disagreement.

Station	State of tide with which the Maximum surge is associated		
	Theory	Observation	Comparison
Ste-Anne-des-Monts	H–F	F	A
Baie-Comeau	H–F	H	A
Pointe-au-Pere	H–F	R–H	N
Tadoussac	H–F	R–H	N
Rivviere-du-Loup	L–R	L	A
St-Joseph-de-la-Rive	L–R	H–R	N
St-Jean-Port-Joli	L–R	H	D
St-Francois	L–R	L–R	A
Quebec City	L–R	L	A

Table 4.11: Tidal range and maximum amplitudes of positive and negative surges in the St. Lawrence Estuary

Station	Spring tidal range (cm)	Amplitude maximum positive surge (cm)	Amplitude of maximum negative surge (cm)	No. of occurrence of positive surges with amplitude ≥ 180 cm during the period 1965–75[a]	No. of occurrences of negative surges with amplitude ≥ 130 cm
Ste-Anne-des-Monts	347	180	140	2 (24)	2
Baie-Comeau	402	290	130	2 (15)	8
Pointe-au-Pere	460	300	130	2 (2)	5
Tadoussac	519	300	160	5 (11)	16
Rivviere-du-Loup	567	300	180	3 (3)	21
St-Joseph-de-la-Rive	695	300	250	5 (29)	20
St-Jean-Port-Joli	573	190	180	4 (34)	33
St-Francois	686	240	230	17 (100)	93
Quebec City	580	300	210	32 (157)	20

[a] Value in parentheses is number of occurrence for ≥ 130 cm.

The results of PROUDMAN (1957) can be summarized as follows: (a) for a long estuary, for a tide of progressive wave type, maximum surges are associated more with low tide; (b) for a long estuary, for a tide of standing wave type, maximum surges are associated more with high tide; (c) for a short estuary, maximum surges are associated more with high tide. PROUDMAN'S results were reinterpreted (with justification) to read low tide (or rising tide) and high tide (or falling tide) wherever "low tide" or "high tide" appears in the above statements.

The nature of the tide in the section between Sept-Iles and Tadoussac is more of a standing wave type than of a progressive wave type, whereas between Tadoussac and Quebec City the tide is more of a progressive wave type. The cumulative frequency of surges of given amplitude associated with a given state of the tide for Tadoussac is listed in Table 4.9. Although the theory does not distinguish between positive and negative surges, they are listed separately. Similar tables were prepared (not shown here) for the other stations. The observed and theoretical results are compared in Table 4.10. Some pertinent data on the surges in the St. Lawrence Estuary are given in Table 4.11.

The astronomical tide is quite significant in the northern parts of the east coast of the United States and it becomes less and less important as we proceed south and also along the Gulf coast. The problem of tide-surge interaction has not received much attention in the United States. MURTY (1984) has summarised the results of few tide-surge interaction studies carried out for the east coast of United States.

The degree of importance of interaction between tides and surges in United States depends on the location. The tide, surge, and the observed water level at Atlantic City on November 25, 1950, are shown in Fig. 4.30. It can be seen that the maximum surge occurred almost at the time of low tide (SWANSON, 1976).

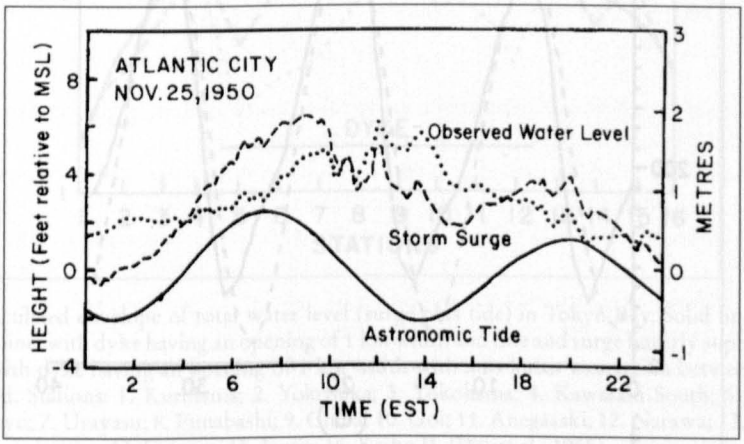

Fig. 4.30: Observed water level, storm surge and astronomical tide at Atlantic City on November 25, 1950. (MURTY, 1984)

4.3.7 China and Japan

Storm surges up to 6 m can occur occasionally on the coast of China, with surges up to 2–3 m occurring frequently. Nonlinear coupling of storm surges and tides is quite pronounced in the shallow water regions of Shanghai on the East China Sea. The mechanism of tide-surge interaction in the coastal waters of China has been investigated by many workers using both analytical and numerical models (CHAI and JINGYONG, 1990; QIN et al., 1994; ZHANG and WANG, 1989; CHOI, 1986; FENGSHU and WENLAN, 1990; YANTING and WANG, 1986, 1990; CHUNYAN, 1990; JINQUAN et al., 1990; YANTING et al., 1992).

More recently QIN and DUAN (1996) have made a detailed study of tide-surge interaction in the coastal water of Shanghai. They used a two-dimensional model to simulate the surge generated by eight tropical cyclones of different tracks crossing the East China Sea

coast near Shanghai. They also analysed in detail the contributions of various nonlinear terms in the dynamic equations to the water levels. Their results show that the nonlinear bottom friction term is of prime importance in controlling the water level and nonlinear tide surge interaction.

Other conclusions drawn by the authors may be summarized as:

(i) Nonlinear tide surge interaction is prominent in coastal waters of Shanghai.

(ii) The simulated storm surges comprising the nonlinear tide-surge effect give better results than pure storm surge simulations both in their peak values and the temporal variations (Fig. 4.31)

(iii) The oscillations with the main tidal period occurring in temporal variation of the water level residuals during tropical cyclone passage are attributed to nonlinear tide-surge interaction.

(iv) Generally the peak surges occur on rising tides whereas they become weaker during the falling tides. This is because of the nonlinear tide-surge interaction.

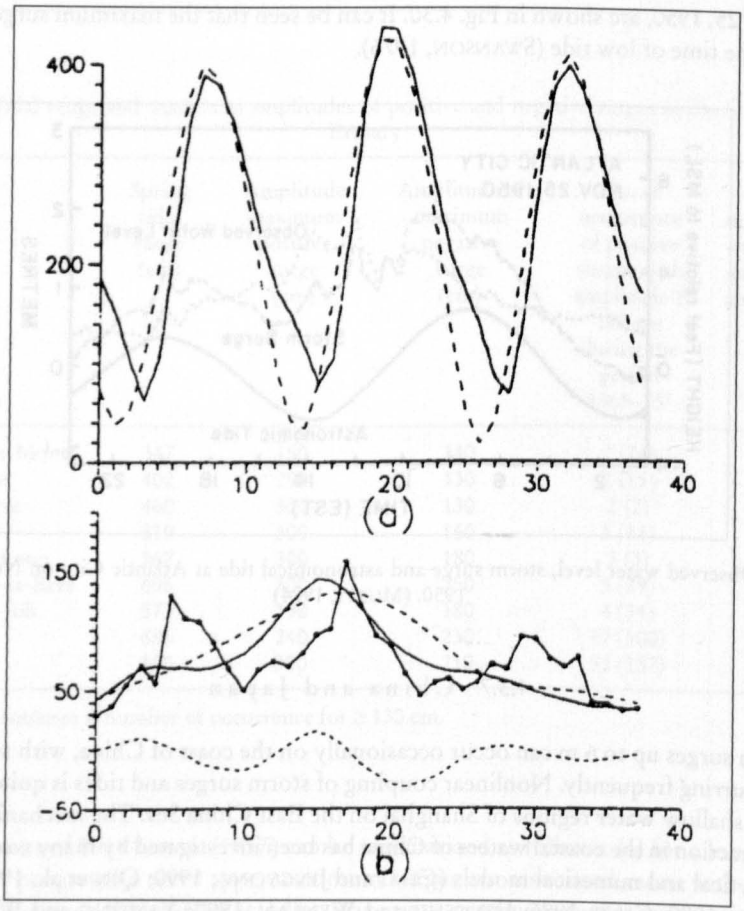

Fig. 4.31: Simulations of tide, storm surge and water level caused by nonlinear T – S coupling during TC Mary (1974). (a) Tide level: solid line – tidal level prediction with 63 constituents (observed), dash line – tidal level prediction with 8 constituents (simulated). (b) Storm surge: solid line with symbols – observed surge, solid line without symbols – simulated surge comprising T – S coupling effects, long dash line: simulated pure surge, short dash line: simulated. (QIN and DUAN, 1996)

Tide-Surge interaction on the coast of Japan is not as important as in China Sea and therefore not many studies have been done in this area. Using two-dimensional numerical model, ITO et al. (1965) studied the problem of tide-surge interaction and the influence of a dyke in Tokyo Bay. Based on the analysis of the results of several runs they conclude that linear superposition of the tide and surge tends to overestimate the total water level (Fig. 4.32).

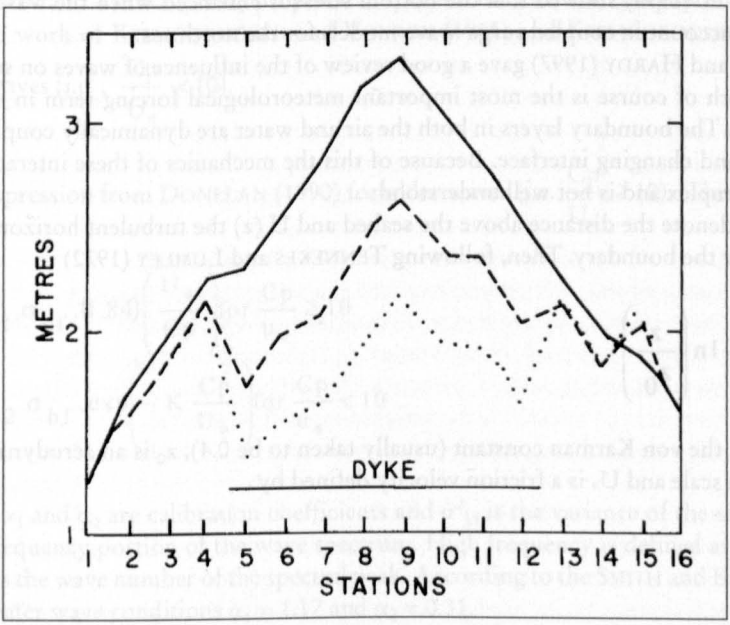

Fig. 4.32: Calculated envelope of total water level (surge plus tide) in Tokyo Bay. Solid line: without dyke; broken line: with dyke having an opening of 1 km width and tide and surge linearly superimposed; dotted line: with dyke having an opening of 1 km width with non-linear interaction between tide and surge included. Stations: 1. Kurihama; 2. Yokosuka; 3. Yokohama; 4. Kawasaki South; 5. Kawasaki North; 6. Tokyo; 7. Urayasu; 8. Funabashi; 9. Chiba; 10. Goi; 11. Anegasaki; 12. Narawa; 13. Kisarazu; 14. Futtusu; 15. Isone; 16. Kaiho II. (ITO et al., 1965)

4.4 Surge-Wind wave Interaction

The state of the art in this field is still evolving and there are at present no universally accepted and definitive approaches. Hence we will discuss the methodologies used by a few different authors.

We start with the excellent review of BODE and HARDY (1997). They point out that the specification of wind stress only as a function of the wind speed – underestimates the very important role played by wind waves in the transfer of momentum across the atmosphere-ocean interface, particularly for tropical cyclones.

These interactions occur through at least the following three mechanisms:

1) Radiation Stress 2) Enhanced Surface Wind Stress and 3) Enhanced Bottom Stress

The Radiation Stress concept, originally proposed by LONGUET-HIGGINS and STEWART (1964) has been used in computing wave set up in storm surge models (e.g., HUBERTZ, 1985).

MASTENBROEK et al. (1993) included radiation stress forcing in a coupled storm surge-wind wave model. They subtracted the gradient of the radiation stress from the wind stress terms in the momentum equations. Their results for the North Sea showed that the contribution from the radiation stress is negligible compared to the contribution from the wind stress. The tide, surge and wind wave components of the water level contribute to the bottom current. The bottom stress depends upon the bottom current in a nonlinear fashion. In shallow water, waves could have a significant influence on the bottom current. WU and FLATHER (1992) and WU et el. (1994) showed that the bottom stress is enhanced when the wave effects are taken into account in coupled surge-wave models for the north sea.

BODE and HARDY (1997) gave a good review of the influence of waves on surface wind stress, which of course is the most important meteorological forcing term in storm surge generation. The boundary layers in both the air and water are dynamically coupled through a moving and changing interface. Because of this the mechanics of these interactions is extremely complex and is not well understood.

Let z denote the distance above the seabed and U (z) the turbulent horizontal velocity profile near the boundary. Then, following TENNEKES and LUMLEY (1972)

$$U(z)=\frac{U_*}{k}\ln\left(\frac{z}{z_0}\right) \tag{4.17}$$

where, k is the von Karman constant (usually taken to be 0.4), z_0 is an aerodynamic roughness length scale and U_* is a friction velocity defined by

$$U_*^2=\frac{\tau_s}{\rho_w} \tag{4.18}$$

where τ_s is the surface and ρ_w is the density of air.

CHARNOCK (1955) suggested that

$$z_*=\frac{gz_0}{U_*^2}=\alpha \tag{4.19}$$

where, α is a constant. This means that z_0 (which is a measure of the aerodynamic roughness) varies linearly with the surface stress τ_s.

Field observations suggest that α is not constant but is dependent on at least the water depth and wave age. The value of α varies from about 0.011 for older or deep water waves SMITH (1980, 1988) to about 0.018 for younger or shallow water waves (WU, 1980, 1982)

Further analysis of field data showed that Z_0 is a function of wave age, usually specified as Cp/U_* where Cp is the wave celerity of the peak frequency and U_* is the friction velocity. Hence

$$z_*=\frac{gz_0}{U_*^2}=f\left(\frac{Cp}{U_*}\right) \tag{4.20}$$

As given by DONELAN (1982), GEERNAERNT et el. (1986) and SMITH et al. (1992). Equation (4.20) was rewritten as

$$z_* = \frac{gz_0}{U_*^2} = \frac{\mu}{Cp/U} \tag{4.21}$$

where, μ is a constant (MAAT et al., 1991)

JOHNSON and VESTED (1992) proposed a hybrid model for the computation of Z_0, following the work of KITAIGORODSKII and VOLKOV (1965) and KITAIGORODSKII (1973) for younger waves (i.e., $\frac{Cp}{U_*} < 10$).

With an expression from DONELAN (1990) for older waves (i.e. $\frac{Cp}{U_*} \geq 10$). This leads to

$$Z_0 = \begin{cases} \alpha_1 . \sigma_{hf} . (1.84) \left(\frac{U_*}{Cp} \right) \text{for } \frac{Cp}{u_*} \geq 10 \\ \alpha_2 . \sigma_{hf} . \exp \left(-K \frac{Cp}{U_*} \right) \text{for } \frac{Cp}{u_*} < 10 \end{cases} \tag{4.22}$$

Here α_1 and α_2 are calibration coefficients and σ^2_{hf} is the variance of the sea surface in the high frequency portion of the wave spectrum. High frequency is defined as $K > 1.5\ K_p$, where K_p is the wave number of the spectral peak. According to the SMITH and BANKE (1975) for deep water wave conditions $\alpha_1 = 1.17$ and $\alpha_2 = 0.31$.

This means that the drag coefficient is a function of wave age, wave height and water depth. MASTENBROEK et al. (1993) examined the effect of waves on the drag coefficient. Instead of parameterizing the dimensionless roughness coefficient, they followed the theory of JANSSEN (1991), which hypothesizes that close to the water surface waves contribute separately to the surface shear stress. Thus

$$\tau_S = \tau_t + \tau_W \tag{4.23}$$

Where τ_t is the turbulent shearing stress and τ_W is the wave-induced stress.

This τ_w changes the boundary layer in the air close to the surface, so that the velocity profile assumes a modified logarithmic form.

They coupled the surge and wave models dynamically, and their results were significantly greater surges than would be obtained by using the drag coefficient of SMITH and BANKE (1975).

However, the disappointing point is that, instead of these more complicated computations, a simple increase of the drag coefficient of SMITH and BANKE (1975) would have given same results.

Approach by Yamashita and Watson

During surges there are complex mutual interactions between wind, waves and currents. The wind generates waves, which influence the wind drag coefficient and hence the wind-driven currents and the surge height. In turn, the currents influence the wave field and the waves influence the wind field. In order more accurately to predict surges, waves and flooding, a thorough understanding of these air-sea interaction processes is important.

The relation between mean wind and wind stress and the influence of waves on this relationship is investigated using data from a new observation tower about 2 km offshore in Tanabe Bay. This measures wave elevation, 20-m wind and 10-m depth current in about 30 m of water. Wind stress and drag coefficient estimates are made using the inertial dissipation method. Data taken during a typhoon are found to show enhanced stress compared with values from empirical formulae in the literature.

For storm surge modelling, the most important forcing terms are the atmospheric pressure, the surface wind stress and the bottom friction stress. The former is of course theoretically well defined and depends only on a reasonably accurate knowledge of the relevant time-dependent pressure field. The stress terms however are not so simple and are normally represented using empirical approximations. These are based on what data are available, which are rather limited and scattered. There is much room for improving our physical understanding of these stresses and then the accuracy of the corresponding forcing terms.

One current area of research is the influence of waves, on both wind stress and bottom stress. Waves are a crucial and complex part of the process of momentum transfer between air and sea, involving the two-dimensional wave spectrum wave growth and decay, non-linear interactions and wave breaking. A forcing term in which the surface stress is a simple function of wind speed is a useful first approximation, and produces acceptable results in many circumstances. However, it is certainly oversimplified and there may be important cases where it is inaccurate, especially in situations where the wind is rapidly changing (such as in tropical storms), near the coast where the water is shallow and the waves fetch-limited, or where the wave spectrum has more than one significant component. Such cases could potentially be more accurately represented by a theory, which correctly accounts for momentum transfer between wind and waves, and between waves and the mean current.

Another effect of waves, which may be important in some circumstances, is their influence on the bottom, stress. In shallow water, wave orbital velocities can be quite large and the flow over the rough bottom produces turbulence. This increases the eddy viscosity experienced by the mean flow and thus the force acting between the mean flow and the bottom.

Using a wave model to predict wave conditions during surge generation, and then modifying the surface may estimate the effect of these processes on surge models and bottom drag coefficients, depending on appropriate properties of the local wave spectrum as outlined below.

The mean force acting on the surface of a body of water due to wind stress is usually approximated as

$$\bar{\tau}_s = \rho_a C_{D10} \bar{U}_{10} | \bar{U}_{10} | \qquad (4.24)$$

where, $\bar{\tau}_s$ is the wind stress at the surface (the horizontal force per unit area acting on the surface), ρ_a the air density, $\bar{U}_{10}$ the mean wind at 10 m and C_{D10} the drag coefficient for wind at 10 m.

With a constant drag coefficient, this formula is found to be reasonable for airflow over

solid rough surfaces. However, as wind speed increases over the sea, the waves get bigger and the surface gets rougher. Thus, for eq. (4.24) to be useful, the drag coefficient must be allowed to vary with wind speed: $C_D(U)$.

For fully developed seas in which the waves are approximately in equilibrium with the local wind, observations of wind stress as a function of wind speed have led to several empirical relations for C_D (U). The data are scattered, but the relationships resulting from the various datasets are all quite similar. Four examples of such formulae are listed in Table 4.12. Note that these data mainly apply to wind speeds greater than about 5–10 ms^{-1}.

However, these results only apply to well-developed seas in deep water. Higher values of C_D found both in growing waves, such as during the onset of a storm and in shallow water. Both of these conditions are necessary for the development of a storm surge, so the effect is potentially important. However, what field data exist are hard to interpret, because the effect is comparable in size with measurement errors, and therefore cannot be determined very accurately. It has not so far been possible to derive any empirical relationship between wind stress and wave conditions, based on the data.

JANSSEN (1991) considers the extra momentum extracted from the wind by growing waves, and then passing into the mean flow. This enhancement of momentum transfer effectively increases the drag. An important parameter here is the ratio of dominant wave phase speed to wind speed, known as the wave C_p/U, which is a measure of whether or not the wind and waves should have reached equilibrium. The effect is not usually incorporated in surge models, and it is uncertain how significant it may be.

The mean retarding force acting on a body of water due to bottom friction is usually approximated as

$$\bar{\tau}_b = \rho_w C_{Db} \bar{u} |\bar{u}| \qquad (4.25)$$

where, $\bar{\tau}_b$ is the bottom stress, ρ the water density, $\bar{u}$ the wave-averaged bottom current and C_{Db} a bottom drag coefficient. For many applications, it is found good enough to use a constant value for C_{Db}.

In shallow water, wave-induced flow near the bottom results in an increase in turbulence. Amongst other things, this increases the rate of vertical transfer of horizontal momentum, and hence the mean drag force between the water and the seabed. This is represented theoretically as an increase in eddy viscosity (which parameterizes the effect of small-scale turbulence in increasing the shear stresses) and hence of the drag coefficient in eq. (4.25).

MASTENBROEK (1992) estimated the size of this effect for storm surges in the North Sea using the relationship between drag coefficient and significant wave height, $C_{Db}(H_s)$. He found that in some shallow areas it could significantly affect the predicted surge, more so than the effect of a wave-dependent wind drag coefficient. However, the size of this effect is similar to that of geographical variations in C_{Db} due to variations in bed roughness. This makes practical implementation difficult because of the lack of sufficiently detailed data on bed roughness.

It should also be pointed out that another effect of waves on local water level at the coast is that of wave set-up. Depending on the beach topography and wave conditions, this can sometimes raise sea level within the surf zone by up to about 1 m. It is an effect that should also be taken into account when considering the flood risk during storms and surges.

The Kyoto University Disaster Prevention Research Institute's Tanabe-Nakajima Storm Surge Observation Tower is located in 30 m of water about 2 km from the coast near Tanabe, in southern Honshu Island, Japan (Wakayama Prefecture). The tower stands at the mouth of

Tanabe Bay, on a plateau of about 10 m depth, around 100 m in diameter, in an area where the depth is predominantly 30 m. It is possible that this plateau will have some local influence on the waves, but it is difficult to determine. The site is in the approaches to the densely – populated area around Osaka Bay. Typhoons regularly cause surges in this area and defenses against these form a significant element of coastal engineering works.

The main instruments of interest here are a 3-component ultrasonic anemometer at about 20 m heights, and a downward-looking ultrasonic wave gauge. Data are recorded at 20 Hz during 20 minutes of each hour. There is also an electromagnetic current meter at a depth of 10 m.

Following YELLAND et al. (1994), wind stress was estimated from the anemometer data using the turbulent (or inertial) dissipation method. This is one of the two commonly used methods, the other being the direct, or eddy-correction method. The latter was also attempted but it was found that 20-minute data samples were not long enough to give convergent results.

The turbulent dissipation method is based on the assumption of a cascade of energy from lower to higher frequencies, at a rate, which is governed, by the rate of dissipation of energy by turbulence at the high-frequency end of the spectrum. The turbulence is assumed to be "frozen", i.e. the time scales are slow compared with the time scale of advection past the observation point. These assumptions yield:

$$S(f) = K\varepsilon^{2/3} f^{-5/3} \left(\frac{U}{2\Pi} \right)^{2/3} \qquad (4.26)$$

where, S(f) is the power spectrum of the down-wind component, K is the 1-D Kolmogorov constant, taken as 0.55, and ε is the high frequency turbulent dissipation rate. If the measured spectrum is found to obey the $f^{-5/3}$ law reasonably well, then an average value of $S(f)f^{-5/3}$ over an appropriate frequency range (0.8–2.0 Hz was used here) may be used in (4.22) to estimate ε. The wind stress τ is then estimated from

$$\tau = \rho (k_v \varepsilon z)^{2/3} \qquad (4.27)$$

where, k_v is the von Karman constant (here taken as 0.4), z is the measurement height (20 m). The drag coefficients is then obtained from (4.20) after correcting the observed mean wind to an estimated value at 10 m using the relation for a logarithmic boundary layer,

$$\frac{U(z)}{U(10)} = \frac{\ln(z/z_0)}{\ln(10/z_0)} \qquad (4.28)$$

where, z_0 is the roughness length $z_0 = e^{-k_v \sqrt{C_D}}$. It should be noted that (4.26) applies to neutral atmospheric stability. A correction is possible for non-neutral conditions, but was found to be small in this case.

The final estimates of wind stress for 29th Sept 1994, excluding the data from 22:00 and 23:00 are plotted against mean wind speed in Fig. 4.33. The four empirical relations from Table 4.12 are plotted for comparison. Particularly at intermediate wind speeds (5–15 ms^{-1}), the data lie well above these curves. These data appear to be an example of departure from

the standard formulae and are thus worthy of further investigation. There is no obvious trend with wind speed, and as with other such data, they are rather scattered. If anything, these data suggest that a constant drag coefficient may be appropriate in this instance. The mean value is 2.2×10^{-3}. However, this is only a small amount of data and it will be necessary to examine a larger amount, including normal wind conditions, in order to draw firm conclusions.

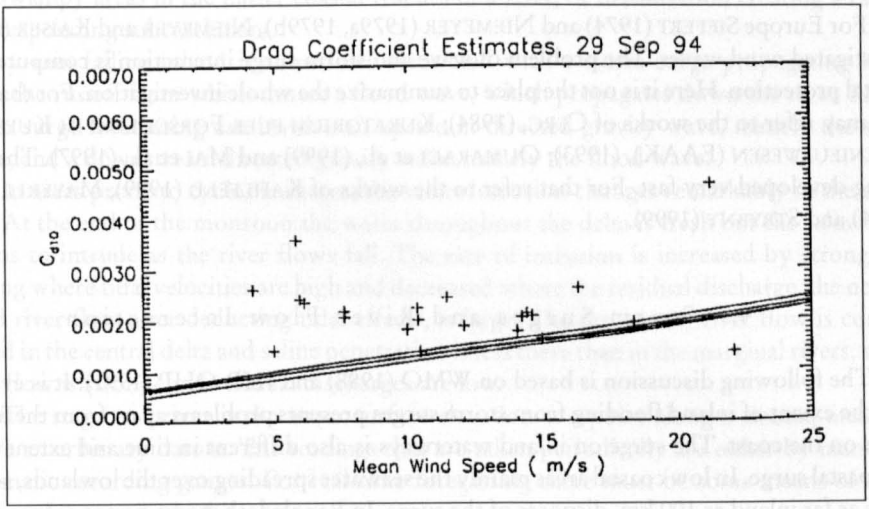

Fig. 4.33: Drag coefficient estimates against wind speed during the typhoon. (YAMASHITA and WATSON, 1997)

The next stage of this work, in addition to further analysis of the wind stress data, will be to incorporate wave effects into a surge model. The first step is to use an ocean wave model to predict the time-dependent wave field during the storm. This has been done for the cyclone, which struck Bangladesh in April 1991, causing a severe disaster in which 150,000 people died. The model is that of YAMAGUCHI et al. (1979) and is a second-generation model, whereas third generation models, which include a more accurate calculation of non-linear interactions, such as WAM, are now available. However, it is uncertain whether this would be any more applicable in the highly nonlinear situation in the extensive shallow region near Bangladesh, and so the more convenient second-generation model was used. Qualitative differences are not expected.

The calculation gives contours of significant wave height during the approach of the cyclone, with a maximum of 15 m being predicted near the cyclone centre. The next step will be to take the results for wave height and use them to modify the surface and bottom drag coefficients in the surge model, as outlined above. In this way the size of wave effects on the surge prediction will be accessed.

ZHANG and LI (1996) have implemented a coupled wave-surge model using JANSSEN's theory for the effect of waves on wind stress, including radiation stress terms, but not considering the effect of waves on bottom stress.

Table 4.12: Empirical Formulae for Wind Drag Coefficient as a function of Wind Speed. (From YAMASHITA and WATSON [1997])

YELLAND and TAYLOR (1996)	$C_{D10} = (0.60 + 0.070U_{10}) \times 10^{-3}$	$U > 6$ ms^{-1}
SMITH et al. (1992)	$C_{D10} = (0.66 + 0.072U_{10}) \times 10^{-3}$	(HEXOS data)
ANDERSON (1993)	$C_{D10} = (0.49 + 0.071U_{10}) \times 10^{-3}$	
SMITH and BANKE (1975)	$C_{D10} = (0.63 + 0.066U_{10}) \times 10^{-3}$	

For Europe SIEFERT (1974) and NIEMEYER (1979a, 1979b), NIEMEYER and KAISER (1997) investigated wind waves. The problem of wave and storm surge interaction is computed for coastal protection. Here it is not the place to summarize the whole investigation. For that readers may refer to the works of CERC, (1984); KURATORIUM FUER FORSCHUNG IM KUESTENINGENIEURWESEN (EAAK), (1993); OUMARACI et al., (1999) and MAI et al., (1997). The modeling developed very fast. For that refer to the works of KAHLFELD (1999), MAYERLE et al. (1994) and STRYBNY (1999).

4.5 Storm Surges and River Flow Interaction

The following discussion is based on WMO (1988) and IHP-OHP (1991). It is evident that the extent of inland flooding from storm surges presents problems apart from the actual surge on the coast. The surge on inland waterways is also different in time and extent from the coastal surge. In low coastal areas mainly the seawater spreading over the lowlands, sometimes as far inland as 100 km, disposes of the surge. In Bangladesh storm surges are reported to reach as far as 160 km inland in recent times. The invasion of the surge water into the marshes creates and expands open bodies of water. The waves, generated by the wind over these bodies, help to transport greater amounts of water inland. The return of this water to the sea is a slow complicated process.

The seiches in inland lakes must be taken into consideration along with the surge to determine flooding possibilities.

As more industries and people continue to move into coastal areas subject to flooding, the determination of the extent of inland flooding becomes increasingly important for the protection of life and property. It is also becoming more difficult to determine the extent of the flooding. The continual construction or changing of levees, canals, navigable waterways, drainage, protective barriers, and other factors, contribute to the complexity of the inland inundation problem. Further complications arise by the changes, which occur in the maze of levees. Natural changes, erosion and subsidence take their toll; also pilfering of the fill or actual cutting of the levees weakens the systems.

An important distinction arises between the tropical and extra-tropical situations; although much more intense, the rainfall flooding arising from tropical cyclones are much more limited in extent than the low-pressure systems associated with extra-tropical surges. Thus, only small regions adjacent to landfall will affected, but this response will very probably coincide with the most severe portion of the surge. If coincidence occurs in the larger, longer lag-time basins affected by extra-tropical low-pressure systems, it is probable that the cause of the flood was due to an earlier event.

Thus the following sets of conditions can be listed as criteria for joint fluvial and surge flooding (WMO, 1988):

(a) In small islands subject to hurricanes, such as the Philippines, Japan and the West Indies, where river response times are short;
(b) Where antecedent conditions have predisposed a larger river to flood and this coincides with a sea surge. This can occur in both tropical and extratropical locations. As an example of the former, a stationary front often lies over Japan in September and early October; the saturated conditions and regular rainfall, often intensified by a typhoon, lead to regular coincidences of floods and surges;
(c) Where human activities have shortened the lag time. Examples are reclamation of the swampy areas in the flatter coastal reaches of a river, or urbanisation creating a rapidly responding subcatchment.

Heavy rain falling inland is sometimes associated with a storm surge propagating into a river, the runoff from which causes a flood wave, which propagates down the river. Hence, storm surge forecasting can involve an upstream-directed gravity wave, namely the storm surge, and a downstream directed gravity wave, namely the flood wave.

In areas prone to cyclonic surges, the saline intrusion changes remarkably in the estuaries. At the end of the monsoon the water throughout the delta is fresh but the saline front begins to intrude as the river flows fall. The rate of intrusion is increased by strong tidal mixing where tidal velocities are high and decreased where the residual discharge, the net seaward river flow after deducting tidal effects, is large. The dry season river flow is concentrated in the central delta and saline penetration is less there than in the marginal rivers, where tidal flow is strong- and residual discharges are low.

The stage of a river is the water surface elevation at a point along a stream, measured above an arbitrary datum. The readings that are taken periodically are either by manual or automatic recording gauges. For real-time forecasting there must be some means of transmitting the stage to the forecast centre.

If required, the stage is converted to a discharge by a stage discharge relationship (often termed the rating curve). A regular programme of current measurements of simultaneous flow and stage observations calibrates the relationship. Such a curve is approximately parabolic, or else linear, on double logarithmic paper. Detailed guidelines on observational practices are to be found in many textbooks and manuals including the WMO Guide to Hydrological Practices.

In a tidally affected river the uniqueness of the stage discharge relationship will be lost. However, it is often possible to construct an approximate relationship for a given downstream stage if a sufficient number of current measurements is available and the estuary level is also read simultaneously.

Efforts should also be made to derive a roughness coefficient for the river. This will be required for the models to be described in subsequent chapters. Again, techniques for this are to be found in hydrometric manuals such as the WMO Manual on Stream Gauging (WMO, 1988).

Tropical cyclones produce large amounts of rainfall. Extra-tropical surges also are associated with rain-producing weather systems. While rain does not have a direct influence on the surge magnitude in the sea, its influence on the river and its coincidence with the sea surge can create critical conditions.

Statistical information required for design work is obtained from climatological reports. Information should include depth-duration-frequency data, areal reduction factors and temporal patterns of past major events.

Rivers are small compared with the adjacent ocean region. The tidal energy of the river can therefore be regarded as originating in the estuary and arriving at the river mouth as a

specifiable boundary condition. The theory that has been applied has related mainly to idealised estuaries and has discussed the surge in terms of standing waves, progressive waves or possible resonance effects. As a general statement, frictional damping becomes the dominant influence in long narrow shallow water bodies. This is the factor most difficult to assess accurately hydrodynamic computer models as well as in empirical formulations.

If water levels fail to respond to upstream floods then the location is tidedominated. Conversely, river domination can be assumed for a location with no response to the flows.

4.5.1 Elbe Estuary (Germany) as case study

The following is based on IHP-OHP (1987, 1991) using SIEFERT (1978b, 1979, 1991) and SIEFERT and HAVNOE (1989).

The concept for understanding the dynamics of storm surges is very simple: Storm surge behaviour in a river is treated as a problem of combination of boundary values and eigenvalues. To solve these problems mathematically, a lot of differential equations have to be solved. Alternatively a hydraulic model (including all eigenvalues) with variation of the boundary values can be applied. This was done for the Elbe (for 200 long river-km) with special respect to Hamburg (Fig. 4.34) and consequently transferred to other rivers (Fig. 4.35).

It turned out that all other influences than astronomical result in a special, individual surge curve in the estuary. Thus we have to consider only two curves as seaward boundary values: the (more or less regular) tide curve and the (irregular) surge curve. These have to be combined with the eigenvalues of the tide-river dynamics. The latter can be considered constant during individual storm events. They are mainly changed by man (deepening and widening of fair-way, course corrections, new dyke lines, weirs, dams, sluices etc.) and are varying through the decades. The upper boundary value (discharge) can also be treated as constant during a surge.

The identification of the seaward boundary values is done by separation of the astronomical or (in first-order approximation for this area) of the mean tide and the surge (Fig. 4.36).

In a first step of approximation the surge curve was characterised by 5 parameters as shown in Fig. 4.37. After these treatments it was investigated how these curves behave when they proceed in a river, and especially, how they interact.

Correlations between storm tide elevations at different locations along a tidal river show no significant coherence. For interpretation of tidal dynamics it is necessary to take into account the complete curves.

IIARLEMAN and LEE give some methods for the solution of tidal propagation in estuaries. The harmonic solution of the linear function equation for the tidal elevation at any x and t

$$\eta = \frac{\eta_0 H}{2} \cdot e^{-\frac{\delta x}{2}} \cdot \left(e^{\mu x} \cos(\sigma t + kx) + e^{-\mu x} \cos(\sigma t + kx) \right) \qquad (4.29)$$

contains the amplitude attenuation coefficient μ or the damping parameter μx.

Using μ and the variation of the damping parameter $d\mu x / dx$ the simple equation for wave propagation in shallow water could be modified to

$$c = S \sqrt{g \cdot d^*} \qquad (4.30)$$

with g = acceleration of gravity d^* = representative water depth in a river

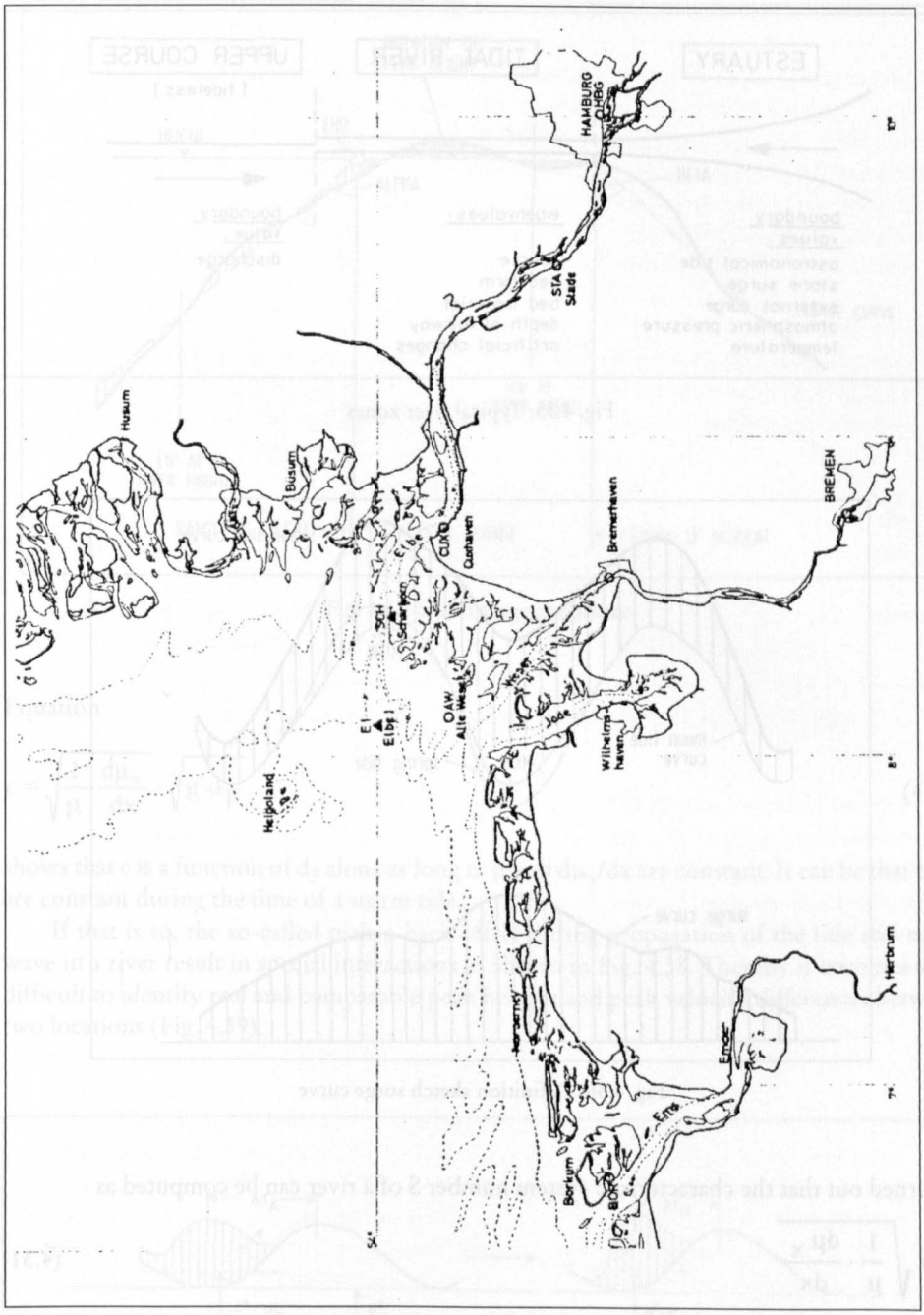

Fig. 4.34: German Bight with Elbe estuary

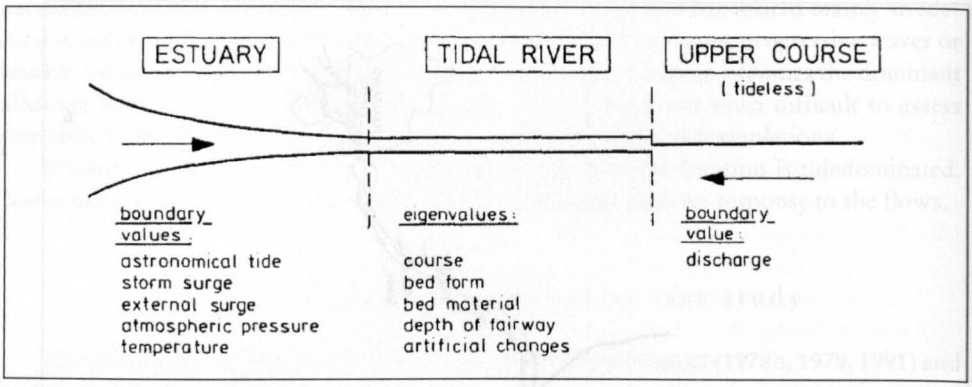

Fig. 4.35: Typical river zones

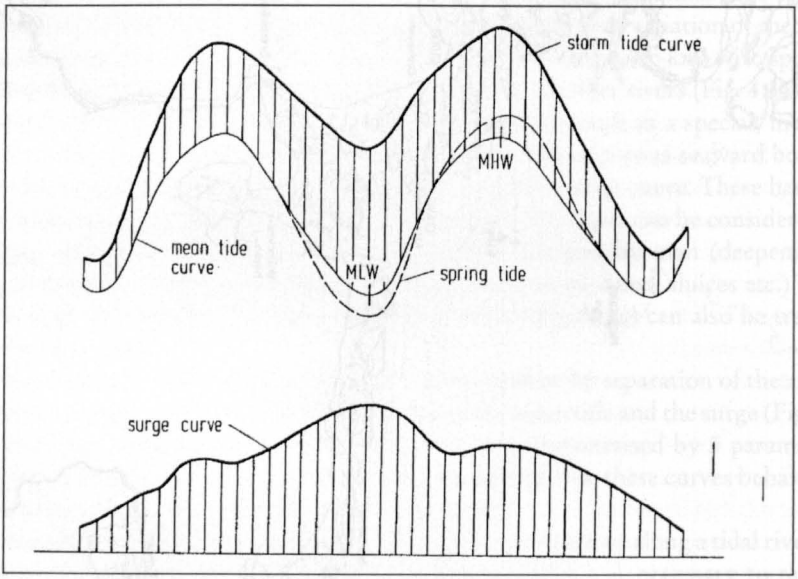

Fig. 4.36: Definition sketch surge curve

It turned out that the characteristic system number S of a river can be computed as

$$S = \sqrt{\frac{1}{\mu} \cdot \frac{d\mu_x}{dx}} \qquad (4.31)$$

The values vary from 0.56 for the Elbe to 1.11 for the Delaware. It changes with time, i. e. with secular changes in the river as was mentioned before.

Computations of a lot of tide and storm surges showed that the "representative water depth" d* in a river is characterised by the depth of the fair-ways d_F. This fact is best proved in rivers with a distinct fair-way of a certain length, as tide and storm surge dynamics are the more concentrated at the fair way the deeper it is, relative to the remaining cross-section.

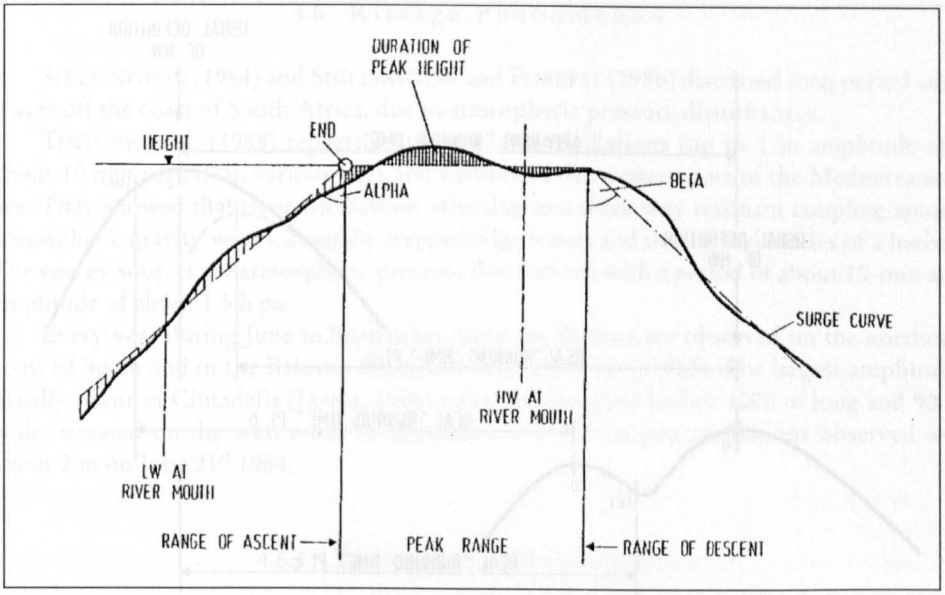

Fig. 4.37: Storm surge parameters

Equation

$$c = \sqrt{\frac{1}{\mu} \cdot \frac{d\mu_x}{dx}} \cdot \sqrt{g \cdot d_F} \qquad (4.32)$$

shows that c is a function of d_F alone as long as μ and $d\mu_x/dx$ are constant. It can be that they are constant during the time of a storm tide.

If that is so, the so-called pick-a-back-effect during propagation of the tide and surge wave in a river result in special interactions as shown in Fig. 4.38. Thereby it becomes very difficult to identify real and comparable peak heights and peak velocity differences between two locations (Fig. 4.39).

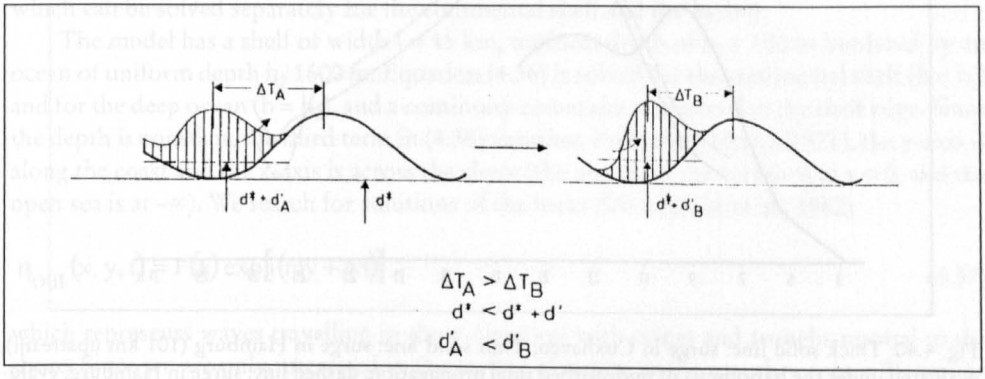

Fig. 4.38: So-called pick-a-back-effect

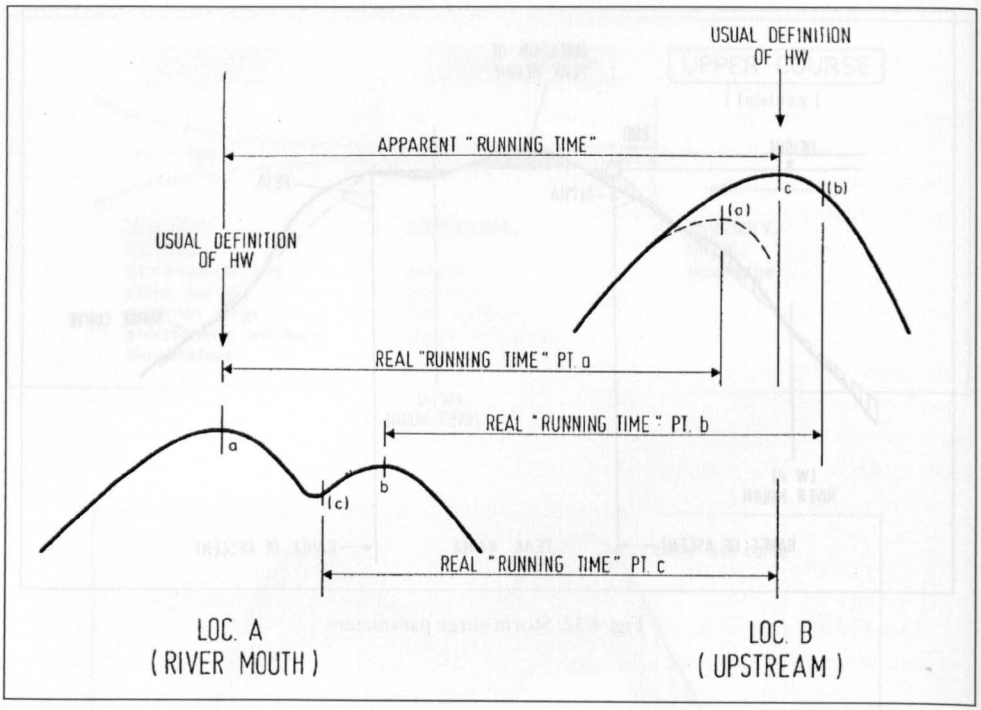

Fig. 4.39: Example of shape variation of the tide curve between two locations

The interactions result in differing propagation velocities not only of the surge, but also of the tide. The shape of the surge curves in Fig. 4.40 may illustrate this. Surges occurred on January 3, 1976, during the highest storm tide ever registered in the Elbe. The comparison of shapes indicates that tidal wave must run a lot faster than usual. As only small alterations of the surge curves are to be expected, best-fit shifts have to be found.

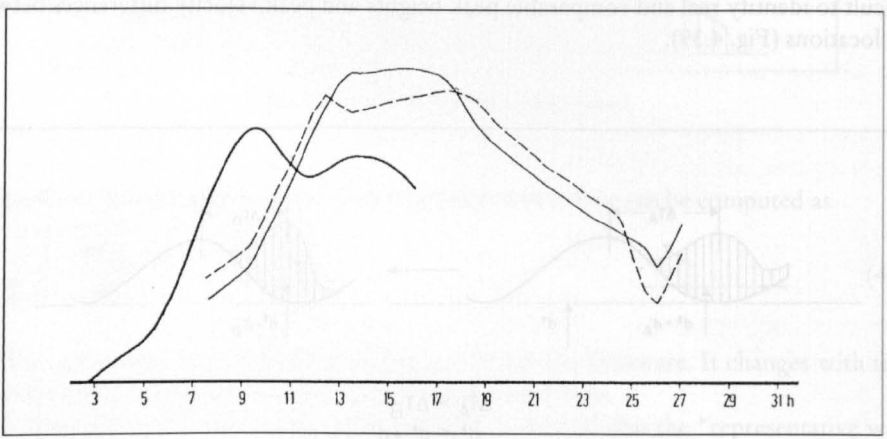

Fig. 4.40: Thick solid line: surge in Cuxhaven; Thin solid line: surge in Hamburg (101 km upstream), evaluated under the hypothesis of undisturbed tidal propagation; dashed line: surge in Hamburg, evaluated under the hypothesis that tidal propagation from C. to H. lasted 3 h instead of the usual 4 h

4.6 Rissaga Phenomenon

SHILLINGTON (1984) and SHILLINGTON and FOREEST (1986) discussed long period edge waves off the coast of South Africa, due to atmospheric pressure disturbances.

TINTORE et al. (1988) reported large sea level oscillations (up to 1 m amplitude and about 10 min period) in various bays and harbors of the western part of the Mediterranean Sea. They showed that these oscillations arise due to a three way resonant coupling among atmospheric gravity waves, coastally trapped edge waves and the normal modes of a harbor. The energy sources are atmospheric pressure fluctuations with a period of about 10-min and amplitude of about 1.5 h pa.

Every year during June to September, these oscillations are observed on the northeast coast of Spain and in the Balearic Islands (RAMIS and JANSA, 1983). The largest amplitudes usually occur in Ciutadella (JANSA, 1986) which is elongated harbor 1000 m long and 90 m wide, situated on the west coast of Minorca one of the largest oscillations observed was about 2 m on June 21st 1984.

4.6.1 Theoretical Explanation

For the theoretical development, we follow TINTORE et al. (1988) closely. The linearlised shallow-water equations for a nonrotating inviscid fluid with variable depth h are

$$\partial u / \partial t + g \partial \eta / \partial x = 0 \tag{4.33}$$

$$\partial v / \partial t + g \partial \eta / \partial y = 0 \tag{4.34}$$

and the continuity equation is

$$\partial \eta / \partial t + \partial (hu) / \partial x + \partial (hv) / \partial y = 0 \tag{4.35}$$

where, u, v are the x, y velocities, η is the surface elevation and g is the gravitational acceleration. Eliminating u and v from (4.33)–(4.35), we obtain the wave equation

$$\partial^2 \eta / \partial t^2 - gh(\partial^2 \eta / \partial x^2 + \partial^2 \eta / \partial y^2) - g \partial h / \partial x \partial \eta / \partial x = 0 \tag{4.36}$$

which can be solved separately for the continental shelf and the harbor.

The model has a shelf of width l = 15 km, uniform depth of h_1 = 100 m bordered by an ocean of uniform depth h_2 1600 m. Equation (4.36) is solved for the continental shelf ($h = h_1$) and for the deep ocean ($h = h_2$), and a continuity constraint is imposed at the shelf edge. Since the depth is constant, the third term in (4.36) vanishes. Following MILES (1971), the y-axis is along the coast and the x-axis is across the shore (the mouth of the harbor is at x = 0, and the open sea is at $-\infty$). We search for solutions of the form (SNODGRASS et al., 1962)

$$\eta_{out}(x, y, t) = F(x) \exp[i(my + wt)] \tag{4.37}$$

which represents waves travelling in the y direction with ridges and troughs normal to the shore. Since we are only interested in the surface elevation at the mouth η_{out} (x = 0), we can replace F (x = 0) by $A_{out.}$

Edge waves are trapped if the phase velocity c is in the range (BUCHWALD and DE SZOEKE, 1973).

$$(gh_1)^{1/2} \le c \le (gh_2)^{1/2} \tag{4.38}$$

For the edge waves trapped in the Balearic Shelf the phase speed must be between 30 ms^{-1} and 125 ms^{-1}. Substitution of (4.37) into (4.36) gives the dispersion relation for trapped edge waves

$$(h_1/h_2)\tan\left[(w^2/gh_1 - m^2)^{1/2} l\right] = \left[\frac{(m^2 - w^2/gh_2)}{(w^2/gh_1 - m^2)}\right]^{1/2} \tag{4.39}$$

Equation (4.39) is solved numerically to obtain the wave number m in terms of the frequency w.

Next we consider the normal modes of the harbor. We solve (4.36) analytically for a rectangular harbor with a constant cross-channel depth and an exponential along-channel sloping bottom of the form

$$h(x) = h_0\{1 - \exp[\alpha(x - L)]\} \tag{4.40}$$

The x coordinate is taken along the channel (the mouth being at x = 0, and the head at x=L) and the y coordinate is across the channel (harbor sides at y = ±d). Values for the harbor of Ciutadella are:

Length = L = 1000 m.
Width = 2d = 90 m.
$\alpha = 4.549 \times 10^{-3}\ m^{-1}$
$h_0 = 5.75$ m.

The following boundary conditions are used: no flow at the side walls, v = 0

At y = ±d, and finite values for the surface elevation and the along-channel velocity at the closed end, η (x = L) and u (x = L). At the mouth, η (x = 0) and u (x = 0) remain undetermined since they must match with the outside solution. We look for solutions of the form (MILES, 1971) and the substitution into (4.36) yields a differential equation for each variable.

$$\eta_{in}(x, y, t) = X(x)Y(y)\exp(iwt) \tag{4.41}$$

The equation for Y (y) is easily solved; applying boundary conditions we obtain

$$Y(y) = C_n \cos[n\pi(y - d)/2d], \qquad n = 0, \pm1, \pm2, \ldots. \tag{4.42}$$

The equation for X (x) is more complicated; after some algebra, it reduces to a special form of Gauss' hypergeometric equation (ABRAMOVITZ and STEGUN, 1965) with two linearly independent solutions expanded about the regular singular point at x = L; because of the boundary conditions one of these solutions must be rejected, and we obtain (LEMON, 1975)

$$X(x) = B\exp\left[\alpha\left(k^2-\sigma^2\right)^{1/2}(x-L)\right]{}_2F_1\{a,b;1;1-\exp[\alpha(x-L)]\} \tag{4.42a}$$

where,

$${}_2F_1(a,b;1;z) = \sum_{j=0}^{\infty}[\Gamma(a+j)\Gamma(b+j)/\Gamma(a)\Gamma(b)j!\,j!]z^j \tag{4.42b}$$

$$a = \frac{1}{2}\left[1+2\left(k^2-\sigma^2\right)^{1/2} \pm \left(1+4k^2\right)^{1/2}\right] \tag{4.42c}$$

$$b = \frac{1}{2}\left[1+2\left(k^2-\sigma^2\right)^{1/2} m\left(1+4k^2\right)^{1/2}\right] \tag{4.42d}$$

$$k = n\pi/2d\alpha \qquad \sigma^2 = w^2/gh_0\alpha^2 \tag{4.42e}$$

The full expression for the free surface elevation for the n^{th} cross-channel mode is

$$\eta_{in}(x,y,t) = \mathrm{Re}\left\{A\exp\left[\alpha\left(k^2-\sigma^2\right)^{1/2}(x-L)\right]{}_2F_1[a,b;1;1-\exp(\alpha(x-L))]\right\} \cdot\cos[n\pi(y-d)/2d]\exp(iwt) \tag{4.43}$$

Note that for a given frequency, both surface elevation and velocity obtained from (4.43) using (4.33) at any position in the harbor are completely determined for each mode except for a constant A_n.

To determine the constant A_n in (4.43), the interior solution has to match the outside coastally trapped wave at the mouth of the harbor. The boundary conditions are continuity of pressure and of mass flux across the mouth.

For a correct matching, the outside edge wave must be expressed in terms of the interior cross-channel modes given by (4.43) (to achieve the matching for the whole hierarchy of modes). However, since the wavelengths of the outside edge waves are much longer than the width of the mouth, we may neglect the excitation of higher cross-channel modes, leaving only the fundamental mode (n=0); the surface elevation will not depend on y. On the other hand, an oscillating free surface in an open basin will radiate energy out into the open ocean. Therefore a complete solution outside the harbor must include the radiated long waves as well as the coastally trapped waves. The matching conditions are

$$\eta_{in}(0) = \eta_{out}(0) + \eta_s(0) \tag{4.44a}$$

$$u_{in}(0) = u_{out}(0) + u_s(0) \tag{4.44b}$$

where, η_s and u_s are the free surface elevation and the offshore velocity for scattered waves.

To account for scattered waves, we followed the equivalent circuit analysis originated by MILES (1971) and modified by GARRETT (1975). In that scheme the sea level elevations at the mouth (m) are taken as voltages inducing a current between the harbor and the open sea. Equation (4.44a) becomes

$$\int_m K_m(y,y')F(y')dy' = \eta_{out}(y) - \int_m K_S(y,y')F(y')dy' \tag{4.45}$$

where, $K_{in}(y, y')$ and $K_s(y, y')$ are respectively the responses of the harbor and the open sea, produces by a point source of transport $\delta(y-y') = hu.n$ at the mouth. Equation (4.45) becomes an integral equation for the velocity distribution across the mouth. However, the exact solution is difficult to obtain. We use a normalized trail function

$$F(y) = I\,f(y) \qquad \int_m f(y)dy = 1 \tag{4.46}$$

Where I is the mass flux at the mouth.

Defining the voltages V as the mean surface elevation across the mouth weighted by the velocity distribution f (y), (4.45) becomes

$$Z_{in} I = V_{out} - Z_S I \tag{4.47}$$

where,

$$V_{out} = \int_m \eta_{out}\, f(y)dy \tag{4.48}$$

$$Z_{in} = \int_m K_{in}(y,y')f(y)f(y')dydy' \tag{4.49}$$

$$Z_s = \int_m K_s(y,y')f(y)f(y')dydy' \tag{4.50}$$

(Z_{in} and Z_s are the impedances of the equivalent circuit). Resonance occurs for maximum fluxes across the mouth. These fluxes can be directly obtained from (4.47).

$$I = V_{out}/(Z_{in} + Z_S) \tag{4.51}$$

Therefore we need to know the voltage V_{out} and the impedances Z_{in} and Z_s.

1. V_{out} is obtained just introducing (4.37) into (4.48). Using the velocity distribution estimated by RAYLEIGH (1945), f (y) = 1/2d.

$$V_{out} = A_{out}\,\sin(md)/m \tag{4.52}$$

where, m (which is a function of frequency) has to be substituted by its value obtained from eq.(4.39).

2. Since the inside solution is known and does not depend on *y*, (4.49) reduces to

$$Z_{in} = V_{in}/I = \eta_{in}(0)/\{2dh_m u_{in}(0)\} \tag{4.53}$$

where, h_m is the water depth at the mouth.

We use (4.33) to obtain u_{in} (L) from (4.43). There is always a phase difference of $\pi/2$ between surface elevation and velocity and therefore (4.53) becomes a pure imaginary number of the form g (w) exp. ($-i\pi/2$) (the sign of g [w] can be positive or negative).

$$Z_{in} = -iw\,\mathrm{Re}[X(0)]/\{2gdh_0(1-\exp[\alpha(x-L)]).\mathrm{Re}[X'(0)]\} \tag{4.54}$$

On a first approximation (without taking Z_s into account), resonance occurs for $Z_{in} = 0$ ($\eta_{in}(0) = 0$). Physically, Z_{in} accounts for the free surface oscillations of a harbor open to an ocean of infinite depth.

3. The problem of scattered waves is solved for an ocean of constant depth h_{out}. The solution is obtained by using Hankel functions as Green's function (MILES, 1971; BUCHWALD, 1971). Using velocity distribution the following expression for Z_s is obtained

$$Z_S = (w/2gh_{out})\left\{1+(2i/\pi)\left[3/2-\Gamma-\ln(wd/(gh_{out})^{1/2})\right]\right\} \tag{4.55}$$

where, $\Gamma = 0.5772\ldots$ is the Euler's constant, and $h_{out} = 100$ m is the depth of the open shelf.

In an equivalent circuit, the real part of Z_s, would be the resistance linearly depending on w. Physically the main effect of Z_s, is to prevent the flux from becoming infinite (Z_s accounts for the energy radiated from the harbor out into the open sea).

However, Z_s, also produces a shift of the resonant frequencies from the frequencies of the harbor free oscillations.

A physical interpretation of (4.51) may be deduced from the above observation on impedances, taking into account that (4.51) is also a time dependent relationship. When $Z_{in} = -\mathrm{Im}(Z_s)$, V_{out} and I have the same time dependency; therefore there is phase difference of $\pi/2$ between η_{in} and η_{out}. On the other hand, when $|Z_{in}| >> |Z_s|$, V_{out} and I have a phase difference of $\pi/2$; therefore η_{in} at the head and η_{out} are in phase if g (w) > 0 and are out of phase if g (w) < 0.

Since we are interested in oscillations with periods of about 10 min, we computed the mass flux through the mouth of the harbor for frequencies lower than 4×10^{-2} rad s^{-1} (T = 2.6 min). Due to the narrowness of the mouth, sin (md)/md •1, evaluation of Z_{in} and Z_s shows that Z_{in} has much higher amplitude than Z_s for most frequencies and it also varies much faster. Consequently,

1. Resonance occurs when $Z_{in} = -\mathrm{Im}(Z_s)$. The location of the resonant peaks depends mainly on the geometry of the harbor and is almost independent of the shelf geometry.
2. The height of the peaks I_{max} depends only on the real part of Z_s, and since this is proportional to w, then $I_{max} \alpha w^{-1}$. Resonant peaks appear at $w = 1.123 \times 10^{-2}$ rad s^{-1} (T = 9.33 min) and at $w = 3.060 \times 10^{-2}$ rad s^{-1} (T = 3.43 min). Coastally trapped waves with these frequencies have wavelengths of 18 km and 5 km, respectively. Their corresponding phase velocities are 33 ms^{-1} and 31 ms^{-1}.

Given the flux at the mouth (I), and dividing it by the cross sectional area, u_{in} (L) can also be obtained from (4.33) and (4.43). Therefore the constant A_0 in (4.43) is determined. For the first frequency peak $A_0 = 300A_{out}$ the surface elevation at the head is 300 times the amplitude of the edge wave. At the mouth of the surface elevation is 3 times the amplitude of the edge wave (the two are not equal at the mouth because of the presence of scattered waves). For example, with an outside wave of amplitude 1cm, we obtain surface elevations of 3 m at the head and a current of about 3 ms^{-1} at the mouth. It is also interesting to note that because of the

phase difference of $\pi/2$, the maximum surface elevation inside the harbor occurs at the zero elevation of the edge wave.

4.6.2 The Work of Monserrat and Colleagues

MONSERRAT and THORPE (1992) summarized the vertical structure of the atmosphere and the synoptic situation during the Rissaga phenomena as follows:

i) Two distinct air masses in the mid and lower troposphere, one cold and humid below and the other warm and dry above, separated by a shallow and usually strong temperature inversion near the surface.
ii) Very weak winds normally from the east or southeast below the inversion veering toward southwest above it.
iii) Strong wind shear at middle levels with a layer of small Richardson number near 500 Mb.

They point out that above meteorological factors while providing a general synoptic situation, cannot fully describe the necessary conditions for gravity wave generation, since the above are not the most dynamically significant factors.

These authors examined the vertical structure of the atmosphere to determine the potential for wave generation by shearing instability and see whether it fulfills the requirements postulated by LINDZEN and TUNG (1976) for the existence of a wave duet to account for maintaining wave coherence.

MONSERRAT and THORPE (1992) considered various source mechanisms and concluded that the vertical profiles of wind and temperature suggest that wind shear is the most likely mechanism. They go onto say that these gravity waves could be trapped modes in a duct and this could be the reason why in certain cases, the waves maintain their coherence for long distances involving at least one full wave-length. RABINOVICH and MONSERRAT (1996, 1998) expanded this study further and included the Kuril Islands also. Fig. 4.41 shows some typical Rissaga type water level oscillations in Japan and China. Figs. 4.42 and 4.43 respectively show the locations of the instruments used in this study for Balearic and Kuril Islands. Fig. 4.44 shows types A, B, C oscillations.

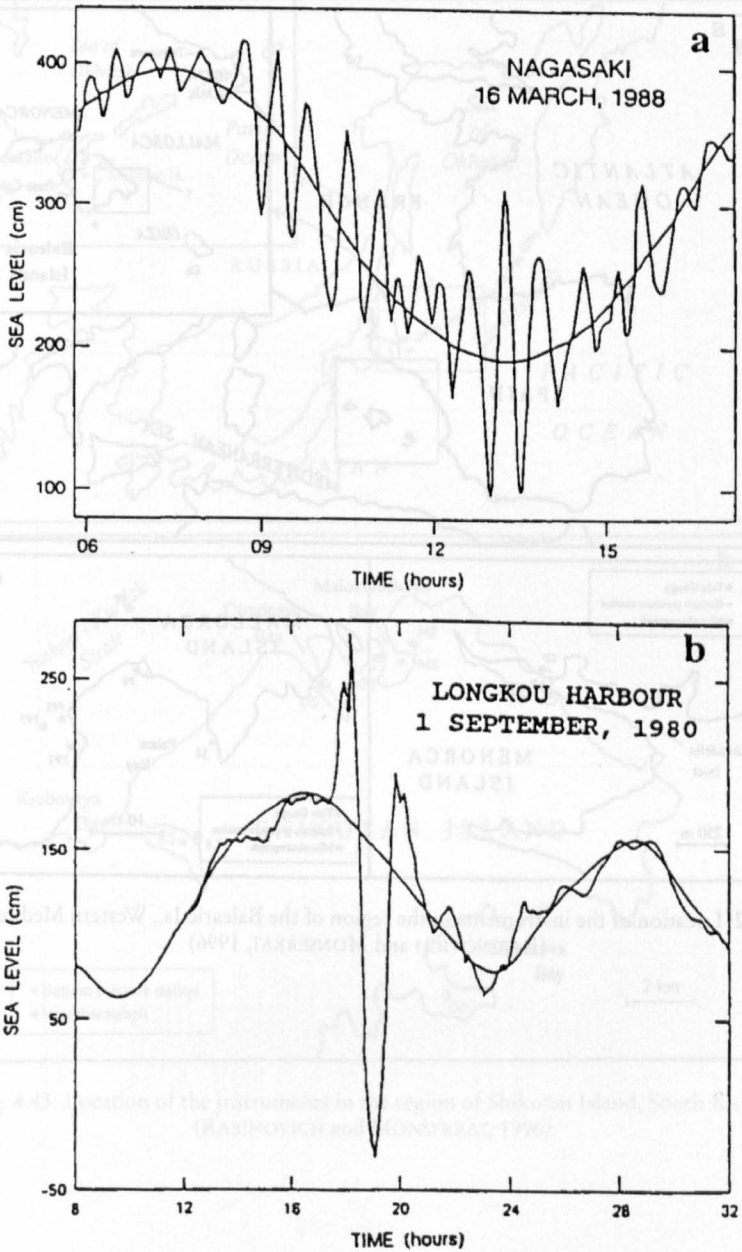

Fig. 4.41: Strong seiche oscillations recorded in Nagasaki Bay, Japan (courtesy of Japan Meteorological Agency) (a) and in Longkou Harbour, China. (WANG et al., 1987) (b)

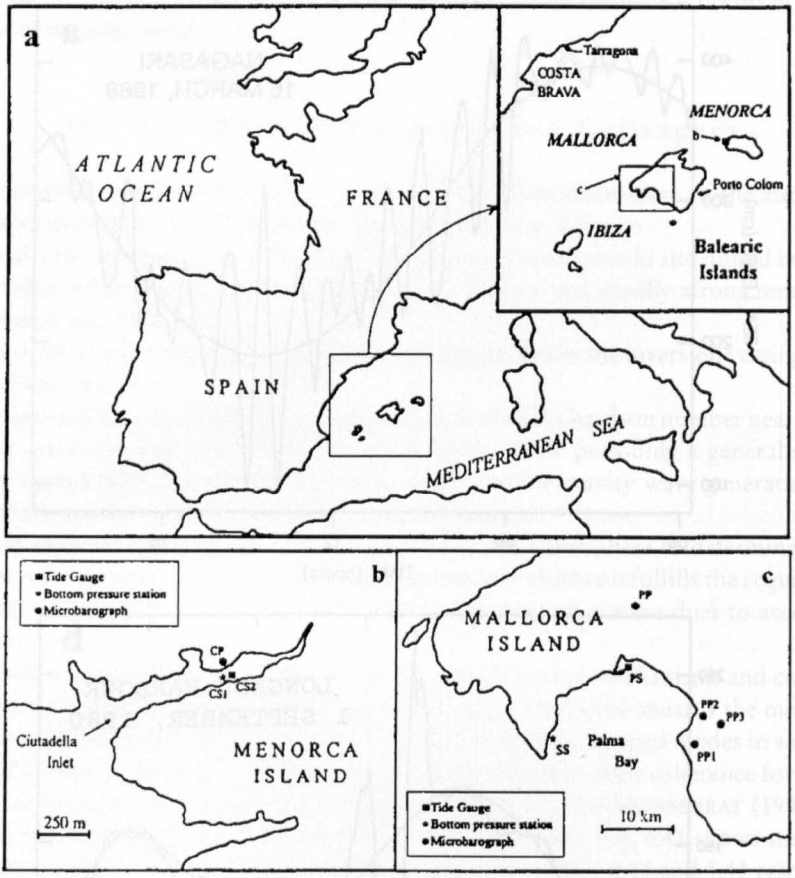

Fig. 4.42: Location of the instruments in the region of the Balearic Is., Western Mediterranean. (RABINOVICH and MONSERRAT, 1996)

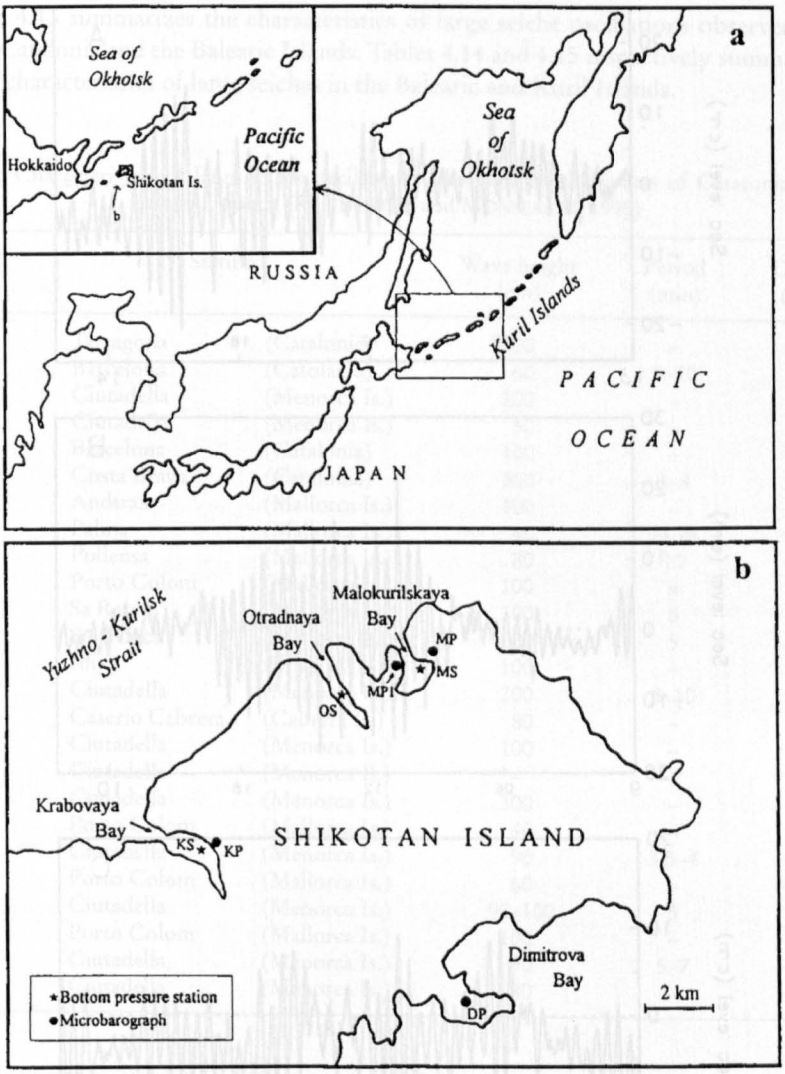

Fig. 4.43: Location of the instruments in the region of Shikotan Island, South Kurils. (RABINOVICH and MONSERRAT, 1996)

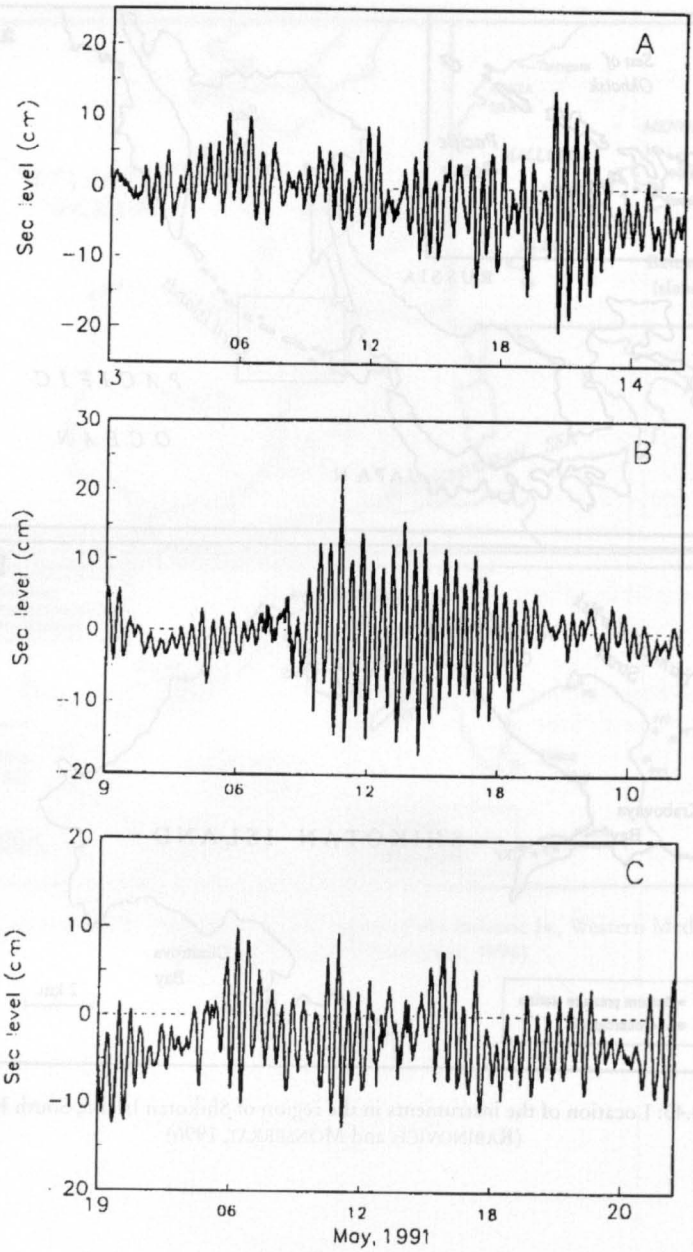

Fig. 4.44: Three recording sections of significant seiches observed in Krabovaya Bay (KS) in May 1991 which may be considered as examples of different types (A, B, and C) of 'seiche events'. (RABINOVICH and MONSERRAT, 1996)

Table 4.13 summarizes the characteristics of large seiche oscillations observed on the coasts of Catalonia and the Balearic Islands. Tables 4.14 and 4.15 respectively summarize the statistical characteristics of large seiches in the Balearic and Kuril Islands.

Table 4.13: Characteristics of large seiche oscillations observed on the coasts of Catatonia and the Balearic Islands (RABINOVICH and MONSERRAT, 1996)

Date	Station		Wave height (cm)	Period (min)	Duration (hours)
11-Jul-72	Tarragona	(Catalonia)	300	–	–
16-Sep-75	Barcelona	(Catolania)	60	8–10	12
16-Sep-75	Ciutadella	(Menorca Is.)	200	–	48
14-Jul-77	Ciutadella	(Menorca Is.)	50	–	–
2-Jul-81	Barcelona	(Catalonia)	100	–	–
2-Jul-81	Costa Brava	(Catalonia)	300	3–4	–
2-Jul-81	Andtrax	(Mallorca Is.)	100	–	–
2-Jul-81	Palma	(Mallorca Is.)	40	14,28	–
2-Jul-81	Pollensa	(Mallorca Is.)	80	10	–
2-Jul-81	Porto Colom	(Mallorca Is.)	100	6	–
2-Jul-81	Sa Rapita	(Mallorca Is.)	100	5	–
2-Jul-81	Sta Ponca	(Mallorca Is.)	200	5	–
2-Jul-81	Ibiza	(Ibiza Is.)	100	–	–
2-Jul-81	Ciutadella	(Menorca Is.)	200	8–10	15
2-Jul-81	Caserio Cabrera	(Cabrera Is.)	80	–	–
18-Jul-81	Ciutadella	(Menorca Is.)	100	–	–
29-Jul-82	Ciutadella	(Menorca Is.)	–	–	48
21-Jun-84	Ciutadella	(Menorca Is.)	300	–	–
14-Jun-85	Porto Colom	(Mallorca Is.)	40	–	–
14-Jun-85	Ciutadella	(Menorca Is.)	90	3.5–4	7
19-Jun-85	Porto Colom	(Mallorca Is.)	60	–	–
19-Jun-85	Ciutadella	(Menorca Is.)	90–100	5	10
3-Jul-85	Porto Colom	(Mallorca Is.)	100	–	2
3-Jul-85	Ciutadella	(Menorca Is.)	90	5–7	8
31-Jul-85	Ciutadella	(Menorca Is.)	80	–	4

Table 4.14: Statistical characteristics of large seiche oscillations recorded in the Balearic Islands in 1989–90 (RABINOVICH and MONSERRAT, 1996)

Event					Stations								
					Ciutadella			Palma			Sol de Mallorca		
No.	Beginning Time		Duration (hours)	Type	Max height (cm)	Mean height (cm)	Mean Period (min)	Max height (cm)	Mean height (cm)	Mean Period (min)	Max height (cm)	Mean height (cm)	Mean Period (min)
	1989												
1	04/07	21:20	63.4	C/A	196.7	39.1	10.7	32.3	14.3	27.5	–	–	–
2	05/08	3:35	19.2	B	126.8	34.2	10.5	23.9	9.3	25.8	10.3	3.7	10.9
3	10/08	20:38	10.2	A	103.8	44.4	11.7	23.5	10.8	25.9	15.1	5.9	15.7
4	31/08	10:58	0.9	C	44.3	38.5	10.8	–	–	–	–	–	–
5	04/09	18:09	4.6	C	64.4	26.2	11.1	–	–	–	–	–	–
6	05/09	5:27	30.0	C	72.8	23.7	10.8	–	–	–	–	–	–
7	07/09	16:40	21.5	C	51.5	18.6	10.3	–	–	–	–	–	–
8	10/09	10:42	7.7	B	95.8	42.4	11.5	–	–	–	–	–	–
	1990												
1	24/09	12:31	4.8	B	66.4	28.5	9.6	–	–	–	–	–	–
2	25/09	12:45	11.5	C	92.8	36.6	10.9	–	–	–	–	–	–

Table 4.15: Statistical characteristics of large seiche oscillations recorded in the region of Shikotan Island in May 1991 (RABINOVICH and MONSERRAT, 1996)

Event					Stations								
					Krabovaya			Otradnaya			Malokurilskaya		
No.	Beginning Time		Duration (hours)	Type	Max height (cm)	Mean height (cm)	Mean Period (min)	Max height (cm)	Mean height (cm)	Mean Period (min)	Max height (cm)	Mean height (cm)	Mean Period (min)
1	09/05	7:14	9.6	B	37.4	21.8	28.6	15.2	5.9	15.4	23.8	9.3	18.3
2	13/05	12:00	12.0	A	34.0	13.8	26.7	15.3	5.7	15.8	21.7	10.8	18.1
3	19/05	6:00	>24.0	C	21.9	8.5	26.1	12.9	3.8	15.1	–	–	–

A key question related to the problem of generation of the *rissaga* phenomenon is the following:

– Why are such strong sea-level oscillations generated in just some specific places?

The stable recurrence of such disastrous events in the same places proves that they are certainly strongly related to the topography and geometry of the correspondingly bays, inlets, or harbors. Ciutadella inlet, Menorca Island (as well as Nagasaki Bay, Japan and some other basins) is just one of such remarkable places. Simultaneous sea-level measurements in Ciutadella inlet and Palma Bay, presented above, demonstrated that during the same events, seiches in Ciutadella are about 6 times larger. What is the reason?

MILES and MUNK (1961) demonstrated that the relative intensity of seiche oscillations in harbours and bays is determined first of all by the Q-factor of the corresponding basin. Reducing the harbour entrance by wave-protection constructions increases the Q-factor and therefore the harbour oscillations. From this point of view it is quite understandable why the narrow inlet of Ciutadella has much stronger seiches than the open-mouthed inlets and harbours in the Balearic Islands with seiches much weaker than in Ciutadella.

GOMIS et al. (1993) tried to explain this fact by the influence of the inlet geometry. They estimated the amplification factor (1) for three inlets in this region (Ciutadella, Mahon and Porto Colom) and showed that in Ciutadella it is much larger than in the other two inlets. But in the region of the Japanese Islands there are several other bays and inlets with this factor no lesser (or even greater) than in Nagasaki Bay although abnormal seiches are known only in the latter basin.

RABINOVICH (1993) proposed that the extreme seiche oscillations observed in some places are forced by some kind of double resonance effect, e.g., by the coincidence of resonant frequencies of the shelf and inner basin, or eigenfrequencies of the harbour and outer bay. The relatively small probability of such coincidences is the main reason of the rareness of basins where large-amplitude seiches are reported.